

Neutrinos via Charm Decays in Astrophysical Sources

by

FRITZ ALI AGILDERE

fritz.agildere@udo.edu

First review: P.D. Dr. Dominik Elsässer (*Technische Universität Dortmund*)
Second review: Prof. Dr. Julia Tjus (*Ruhr-Universität Bochum*)
Submission date: July 25, 2024

Zusammenfassung

Platzhalter

Abstract

Placeholder

Acknowledgements

Contents

1	Introduction	1
2	Background	3
2.1	Particle Physics	3
2.1.1	Fundamental Interactions	3
2.1.2	Hadrons & Leptons	4
2.1.3	Reference Frames	5
2.1.4	Particle Collisions	5
2.1.5	Cooling & Decay	5
2.2	Multimessenger Astronomy	8
2.2.1	Magnetic Field Scales	8
2.2.2	High Energy Cutoff	8
2.2.3	Stochastic Acceleration	10
2.2.4	Cosmic Rays	11
2.2.5	Neutrinos	12
2.2.6	Photons	12
2.2.7	Gravitational Waves	12
2.3	Astrophysical Sources	12
2.3.1	Magnetars	13
2.3.2	Spindown	14
2.3.3	Active Galactic Nuclei	15
2.3.4	Accretion Disks	15
3	Methods	19
3.1	Cross Sections	19
3.1.1	Scattering	19
3.1.2	Production	21
3.2	Spectral Distributions	24
3.2.1	Charm	24
3.2.2	Pions & Kaons	25
3.3	Computation	26
3.3.1	Injection	27
3.3.2	Production & Decay	28
3.4	Implementation	28
4	Results	30
5	Conclusion & Outlook	37
	Bibliography	38

Figures

1	Inelastic cross sections σ_{hp} for hadron-proton scattering.	21
2	Inclusive differential cross sections for $pp \rightarrow D^0 X$ production.	23
3	Magnetar ν flux from c decay including optical depth.	30
4	Magnetar ν flux compared to c decay with optical depth.	31
5	Magnetar ν fluence compared to c decay with optical depth.	31
6	Magnetar ν flux from c decay excluding optical depth.	32
7	Magnetar ν flux compared to c decay without optical depth.	33
8	Magnetar ν fluence compared to c decay without optical depth.	33
9	AGN accretion disk ν fluence from c decay.	36
10	AGN accretion disk ν fluence compared to c decay.	36

Tables

1	Fits to the total cross sections σ_{hp} in hadron-proton collisions.	20
2	Model independent ratio of elastic and total σ_{hp} cross sections.	20
3	Parametrization of the c quark differential cross section.	22
4	Coefficients for c hadron production, cooling and decay.	25
5	Parametrized spectral distribution for π production.	26

Abbreviations

AGN	Active Galactic Nucleus
CMB	Cosmic Microwave Background
DSA	Diffusive Shock Acceleration
EW	Electroweak Theory
FF	Fragmentation Function
GR	General Relativity
GZK	Greisen-Zatsepin-Kuzmin
PDF	Parton Distribution Function
QCD	Quantum Chromodynamics
QED	Quantum Electrodynamics
QFT	Quantum Field Theory
QM	Quantum Mechanics
SM	Standard Model
SMBH	Super-Massive Black Hole
SR	Special Relativity
UHECR	Ultra-High-Energy Cosmic Ray

1 Introduction

In their quest for a deeper understanding of astrophysical phenomena, researchers have moved to investigating a combination of different signal types. This has given rise to the independent field of multimessenger astronomy that studies electromagnetic radiation, cosmic rays, neutrinos and gravitational waves to infer which processes drive their sources [1]. While such environments are likely opaque to photons, charged particles may escape after being accelerated, predicting a non-thermal *Ultra-High-Energy Cosmic Ray* (UHECR) population. Experiments indeed support this expectation by regular measurements of energies from 10^9 GeV up to 10^{11} GeV in accordance with the *Greisen-Zatsepin-Kuzmin* (GZK) cutoff [2]. The question then becomes whether it is possible to reconstruct any source region properties from these signals.

One basic constraint derived from observations of extreme energies is a relationship between the sizes and field strenghts of possible sources [3]. From this follows that plausible candidates for UHECR origins consist mostly of stellar remnants like white dwarfs or neutron stars as well as *Active Galactic Nuclei* (AGN) that are powered by *Super-Massive Black Hole* (SMBH) engines at their center [4–6]. Matching of cosmic ray signals to specific sources, however, proves to be an extremely difficult task because large scale magnetic fields isotropize the directions of charged messenger particles.

This leaves neutrinos and gravitational waves as multimessenger candidates, both of which are the subject of multiple promising discoveries at high-energy detection facilities [7–9]. Although gravitational signals provide valuable insights regarding the interaction and structure of massive objects, they do not carry information on particle acceleration. Neutrinos, on the other hand, are produced in hadronic reactions with proton or photon fields close to the accelerating regions. Their weakly interacting nature allows them to escape and propagate almost freely, making them reliable pointers to their sources [10].

Due to their strong physical connection, the origins of highly energetic neutrinos are thought to be closely related to those of hadronic cosmic rays. Recent combined analyses indicating simultaneous neutrino and gamma emissions from a flaring blazar seem to be in agreement with this assumption for the case of an AGN scenario [11, 12]. More compact sources such as strongly magnetized pulsars are also an area that is being actively researched [13]. The standard approach to modeling these sites starts with injecting protons accelerated by some astrophysical process into a photonic or baryonic target surrounding the potential source. In the resulting interactions, energetic pions and kaons are produced, which then decay to neutrinos. This method is generally self-consistent and capable of producing plausible results, but neglects certain effects that might reveal more detailed information about the respective source.

1 Introduction

When working towards describing sources of neutrinos in the upper UHECR energy ranges, intermediate hadrons must exhibit highly relativistic velocities. Accordingly, these particles experience extreme time dilation, leading to lifetimes appearing several orders of magnitude longer than in their rest frames when viewed from the surrounding fields. If sufficiently high matter densities are present, the typically investigated pions and kaons are therefore scattered to lower energies before decaying to neutrinos. Due to their much shorter lifetimes, more exotic particles, many of which contain at least one charm quark, then become significant contributors to the neutrino flux that would otherwise remain suppressed [14].

The present work estimates the relative neutrino contribution from decays of such charmed hadrons. For this purpose, results of the magnetar case presented in [15] are reproduced before applying the same procedure to a simplified AGN accretion disc model, assessing the feasibility of charm decay dominance in this latter scenario.

Following this introduction, chapter 2 summarizes the core physical concepts relevant to this thesis, including particle physics, multimessenger astronomy, and their connection to the treated astrophysical sources. Building on this background, chapter 3 introduces semianalytical methods involving empirical parametrizations, which are then employed for all further computations. Lastly, chapter 4 presents the results, with chapter 5 providing a concluding discussion as well as potential future prospects based on these findings.

On the topic of unit conventions, this work uses varying styles for different contexts. Physical equations are usually given in Gaussian units, while masses might have natural units of energy when concerning particle physics or be written as multiples of the solar mass in astrophysical settings. To avoid ambiguities, units will be clarified in the text whenever necessary.

2 Background

On their journey through space, messenger particles are subject to various influences, both in terms of type and scale, before reaching our planet. Understanding this propagation requires a thorough comprehension of physical processes at all scales of application, from production in astrophysical sources, through interactions with the vast radiation and matter fields that fill the cosmos, to entering the solar system and ultimately the terrestrial atmosphere. The following sections provide an incomplete overview of aspects relevant to the treatment of this complex topic, as well as references for further study on the various related subjects.

2.1 Particle Physics

In our modern view, interactions and categories of elementary particles are most accurately described by a construct called the *Standard Model* (SM) of particle physics. Underlying this formalism is the mathematical framework known as *Quantum Field Theory* (QFT) that combines and generalizes properties of *Quantum Mechanics* (QM) and *Special Relativity* (SR) to produce a consistent description of microscopic reality. Excitations in the associated fields are referred to as quanta and manifest themselves as observable particles. Since this work is mostly concerned with the statistical behaviour of large quantities instead of individual particle probabilistics, a more detailed treatment is omitted, with the exception of certain phenomena important to the justification of some later assumptions.

2.1.1 Fundamental Interactions

With the theory of *Quantum Electrodynamics* (QED) representing a quantized description of classical electromagnetism, the first successful QFT formulation had been realized. It governs all interactions between electrical charges that involve photons and predicts observations with extremely high precision. Each subsequent QFT is built on a foundation of QED achievements, such as *Quantum Chromodynamics* (QCD) for strong force interactions or the unified framework of *Electroweak Theory* (EWT) that includes both weak force and electromagnetic phenomena.

According to the SM formalism, these interactions are mediated by bosonic elementary particles, namely massless photons γ for electrodynamics or gluons g in case of the strong force sector, as well as massive Z and W^\pm bosons that carry the weak force. The only remaining fundamental interaction not contained in the SM is gravity, the effects of which are currently best described in terms of *General Relativity* (GR) as the continuous macroscopic curvature of spacetime due to the presence of large masses. Because elementary particles exclusively inhabit microscopic scales, their behavior is usually indistinguishable from that described by SR in flat space.

2.1.2 Hadrons & Leptons

In addition to the previously listed gauge bosons, the SM further includes elementary fermions as the fundamental constituents of matter. These sort into the categories of quarks and leptons, both of which are further grouped by generations of quark or lepton pairs. Ordered according to their generation, there are flavors of up and down, charm and strange, as well as top and bottom for quarks, which are denoted by their initial letters. For charged leptons, there exist electrons e as well as the heavier muon μ and tau τ that each have an associated neutrino ν with no electrical charge. This picture is completed by the corresponding antiquarks and antileptons for all particles mentioned above.

Apart from an electrical charge, quarks are also carriers of so-called color charges that couple to gluons, which, in contrast to the electrically neutral photons, carry colors themselves. Gluons are therefore capable of self-coupling, leading to higher binding energies with increasing distances. If removed far enough, this energy is eventually released by producing a quark pair, ultimately leading to the creation of bound color-neutral states.

These resulting composite particles are called hadrons, with the entire process being referred to as hadronization. This naturally leads to the concept of confinement, which states that quarks cannot exist as free particles, with the notable exception of very high energies. In these regimes, strong force coupling becomes small and allows quarks to behave almost freely, defining the term asymptotic freedom. A major consequence of this is that perturbative QCD calculations become possible, which would otherwise require complex approaches such as discrete QCD on a lattice or some type of effective field theory instead.

The quark model enables classification of hadrons based on their constituent numbers. Baryons are comprised of three quarks, all with different colors, while mesons contain two quarks with opposite color and anticolor charges. From spin addition, it is clear that baryons obey fermionic statistics, while mesons act as bosons. Exemplary quark contents are given for baryons such as protons $p \equiv uud$ and neutrons $n \equiv udd$ as well as pions $\pi^- \equiv \bar{u}d$ and kaons $K^- \equiv \bar{u}s$ in the case of mesons. The charmed hadrons considered in this work are the same mesons $D^0 \equiv c\bar{u}$ as well as $D^- \equiv \bar{c}d$ and $D_s^- \equiv \bar{c}s$ with the baryon $\Lambda_c^+ \equiv udc$ as in [15]. Specific decay channels will be listed directly in the relevant sections with [16] providing a broad overview.

Contrary to hadrons, leptons are fundamental particles. Due to being colorless, they are not affected by the strong force, meaning that all leptonic interactions obey EWT instead. Noting that photons only couple to electrical charges, this leaves neutrinos as the only particles which interact exclusively via the weak force. Here, one distinctive feature of the weak interaction should be mentioned as well, namely that of parity violation. This manifests by only coupling to left-handed components of particles and right-handed components of antiparticles. Handedness in this context refers to chirality, which for massless particles is equivalent to helicity or the sign of the spin projection onto the momentum vector. Because the SM assigns zero mass to neutrinos, this EWT property suppresses certain decay modes and enforces correlated polarizations for the involved leptons. Not included in the SM is the observation of neutrino oscillations, which are, however, not relevant for this work, since flavor differences are neglected.

2.1.3 Reference Frames

Depending on the application, energies in particle physics are either given as viewed from a suitable rest frame or independent from the choice of coordinates altogether. One particularly convenient formulation uses incoming and outgoing momenta p_1, p_2 and p_3, p_4 to define

$$s = (p_1 + p_2)^2 \quad t = (p_1 - p_3)^2 \quad u = (p_1 - p_4)^2$$

as the Mandelstam variables, which assign different channels to scattering processes based on the squared momentum carried by an exchanged mediating particle. Implied in this context is a Minkowski inner product, making the above quantities manifestly Lorentz invariant. When working with parametrizations defined for use in different subdisciplines, it regularly becomes necessary to convert from center of mass energies \sqrt{s} to the energy E of a projectile as viewed in the system of a stationary target, where vectors $P = (E, \mathbf{P}c)$ and $p = (mc^2, 0)$ represent the respective particle momenta. With \mathbf{P} denoting a classical projectile momentum and c the speed of light, rest masses M and m for projectile and target lead to a relation $E^2 = \mathbf{P}^2 c^2 + M^2 c^4$ and

$$s = (P + p)^2 = (E + mc^2)^2 - \mathbf{P}^2 c^2 = 2Emc^2 + m^2 c^4 + M^2 c^4$$

for the invariant mass. The trailing terms in this equation become negligible at high energies, allowing for an approximation $s = 2Emc^2$ in the target rest frame.

2.1.4 Particle Collisions

Another important aspect of particle physics is the description of collision processes. For this purpose, the concept of cross sections σ should be understood. In classical mechanics, these quantities are solely related to geometric properties of the objects involved, assuming they only interact upon impact. If longer range forces are included, the cross section represents a larger effective area that measures how the trajectory of an incoming projectile is influenced by the target. Additionally, differential cross sections with respect to some independent variable such as solid angle $d\sigma/d\Omega$ or kinetic energy $d\sigma/dE$ can be defined. Measurements of this quantity often reveal more information about the inner structure of targets. To distinguish these cases, one might refer to σ as the integrated cross section. Since QM is at the core of particle physics, cross sections in this context are instead interpreted as probability measures of fundamentally stochastic collision processes, such as the production of specific particles. It can also be useful to separate cross sections into elastic and inelastic components, especially for collisions in which particles lose energy, as is the case for cooling processes via scattering.

2.1.5 Cooling & Decay

Consider an infinitesimally thin slice of a target medium with particle number density n and volume $V = Sdx$ where S and dx measure surface area and thickness, respectively. Accordingly,

there exist $\tilde{N} = nV$ targets that each have effective interaction cross sections $\tilde{\sigma}$ with a total coverage of $\tilde{S} = \tilde{\sigma}\tilde{N}$ as viewed by an incident projectile.

The probability for dissipating these beam constituent then corresponds to the ratio $\mathcal{P} = \tilde{S}/S$ of both areas or explicitly $\mathcal{P} = \tilde{\sigma}n dx$ in case of dx as the covered distance. Expressing $\tilde{\sigma} = \kappa\sigma$ in terms of the inelastic scattering cross section σ and a dimensionless factor κ called inelasticity, one can identify a length scale $\lambda = (\kappa\sigma n)^{-1}$ as the mean free path between collisions. Multiplying with κ includes the ratio of remaining to initial energy, which is taken to be constant. From this follows a reduction in beam particles $dN = -N\lambda^{-1}dx$ proportional to N as the total projectile count and $\mathcal{P} = \lambda^{-1}dx$ for the reformulated probability which represents an ordinary differential equation of first order. The solution is found to follow an exponential law

$$N(x) = N_0 \exp\left(-\frac{x}{\lambda}\right)$$

where N particles remain over some distance x with N_0 as the initial amount. Furthermore,

$$P(x) = 1 - \exp\left(-\frac{x}{\lambda}\right)$$

gives the probability of a particle having been scattered after travelling x length units. Similar steps for time instead of distance lead to the well known equation

$$N(t) = N_0 \exp\left(-\frac{t}{\tau}\right)$$

describing exponential decay. It commonly appears in the context of radioactive materials but also applies to hadrons and leptons or more generally any quantity which decreases at a rate proportional to itself. Analogous to the previous case, a particle decays with probability

$$P(t) = 1 - \exp\left(-\frac{t}{\tau}\right)$$

before a time t has passed and for τ as the mean lifetime. Translating this from rest frame to laboratory coordinates defines the decay timescale $t_{\text{dec}} = \tau\Gamma$ with a Lorentz factor $\Gamma = E/m$ via projectile energy and invariant mass. This is equivalent to a characteristic decay length given by $\lambda_{\text{dec}} = vt_{\text{dec}}$ where the velocity $v = c$ can be set for highly relativistic particles. Additionally, mean free path and cooling distance $\lambda_{\text{cool}} = (\kappa\sigma n)^{-1}$ refer to exchangeable concepts. Particles lose energy in every collision, which is the same as reducing temperature from a thermodynamics perspective. Dividing by the speed of light c translates this expression to $t_{\text{cool}} = (\kappa\sigma nc)^{-1}$ as a cooling timescale. Analogously, the distance $\lambda_{\text{dec}} = c\tau E/m$ can be rewritten as $t_{\text{dec}} = \tau E/m$ in units of time. Substituting into the decay formula yields a cooling factor

$$C = 1 - \exp\left(-\frac{t_{\text{cool}}}{t_{\text{dec}}}\right) \quad (1)$$

that rescales spectra from direct production to account for decay processes taking place after collisional energy losses have occurred. This is an essential mechanism for the hypothesis that

neutrinos from charm dominate pion and kaon contributions at high energies. While longer lived particles experience significant cooling thanks to time dilation, charmed hadrons decay promptly in comparison, resulting in a neutrino flux that directly traces the underlying hadronic spectrum. One requirement for the validity of (1) is that $\lambda_{\text{dec}} \ll d$ holds, with d measuring the target field size to ensure decays occur exclusive inside this region.

$$\mathcal{O} = \tag{2}$$

2.2 Multimessenger Astronomy

An extension of traditional astronomy, the field of multimessenger astrophysics continues to thrive, providing valuable insights via the combination of complementary information carried by multiple messenger species. This section begins by expanding on physical concepts alluded to in chapter 1 before continuing to describe the available multimessenger candidates in some detail. For a more extensive overview, reference [1] should be consulted.

2.2.1 Magnetic Field Scales

Particles carrying electric charges $Q = Ze$ and moving at velocity v orthogonal to a homogenous magnetic field B are acted on by the Lorentz force $F = QvB$ that produces a gyrating motion. With the elementary charge e and Γ as a Lorentz factor, this must balance a relativistic centripetal force $F = m\Gamma v^2/R$ on the resulting circular path with R giving the Larmor radius. Rearranging and identifying $p = m\Gamma v$ leads to the solution

$$R = \frac{p}{QB}$$

on which the magnetic field extent D imposes $R < D$ as a condition. In case of highly relativistic energies, one can substitute $E = pc$ for the momentum to obtain an inequality $E < QcBD$ from the above considerations. Realistic astrophysical magnetic fields are not ordered, instead following turbulences that travel through the plasma. To incorporate effects of moving scattering centers, a factor β proportional to the Alfvén velocity is included, giving

$$E < Ze\beta cBD \tag{3}$$

as the Hillas criterion. It is named after its description in [3] and connects source region sizes to the strength of prevailing magnetic fields, with observed cosmic ray energies as a constraint.

2.2.2 High Energy Cutoff

At very high energies, protons and nuclei interact with cosmic photons, which can be blueshifted up to extreme gamma regimes due to the Doppler effect. In these processes, the photon spin is absorbed to produce a delta resonance Δ^+ representing an excited proton state. This decays almost immediately to pairs of nucleons and pions, leading to $p\gamma \rightarrow n\pi^+$ or $p\gamma \rightarrow p\pi^0$ as probable

2 Background

reaction channels and resulting in a change of momentum for the produced particles. For the case of *Cosmic Microwave Background* (CMB) radiation, a close to perfect black body spectrum

$$\frac{dn}{d\epsilon}(\epsilon) = \frac{\epsilon^2}{\pi^2 \hbar^3 c^3 (e^{\epsilon/k_B T} - 1)}$$

is given by [17] as the number density. From a CMB temperature of $T = 2.725$ K follows that significant photon numbers exist with energies around $\epsilon = 10^{-12}$ GeV in the CMB rest frame.

To find a threshold in center of mass coordinates, the scalar product is used for

$$s = (p_p + p_\gamma)^2 = p_p^2 + p_\gamma^2 + 2p_p p_\gamma = m_p^2 c^4 + 2E\epsilon = M^2 c^4$$

where $M = m_p + m_\pi$ and $m_\gamma = 0$ as well as head on collisions have been assumed. The solution

$$E = \left((m_p + m_\pi)^2 c^4 - m_p^2 c^4 \right) / (2\epsilon)$$

corresponds to roughly $E = 10^{11}$ GeV for the so-called GZK cutoff. Energies that exceed this value when viewed from CMB coordinates lead to significant losses, making the universe opaque to such protons. If pair production $\gamma \rightarrow e^+ e^-$ from proton interactions is considered, one finds

$$E = \left((m_p + 2m_e)^2 c^4 - m_p^2 c^4 \right) / (2\epsilon)$$

or approximately $E = 10^9$ GeV by setting $M = m_p + 2m_e$ instead. For alpha particles and heavier nuclei, similar steps apply, while electrons are limited mainly through Compton downscattering. Additionally, there exist infrared and radio backgrounds as potentially relevant radiation fields. From the multiple competing mechanisms for energy losses and momentum isotropization, it is as a consequence extremely challenging to reliably interpret cosmic ray signals and practically impossible to reconstruct any information about specific sources.

2.2.3 Stochastic Acceleration

From the introduction of theoretical limits in sections 2.2.1 and 2.2.2 arises the question of how particles reach these high energy regimes in the first place. Due to its relatively simple derivation and surprising accuracy in the description of measured spectra, probabilistic collisions are often viewed as one of the most plausible mechanisms responsible for cosmic ray acceleration. The general case is described in [18] and supposes that for each collision, particles gain some energy proportional to a constant factor η and remain in the accelerating region with probability ς on average. With initial conditions N_0 for the number of particles and E_0 as the mean energy, this results in $N = N_0 \varsigma^k$ and $E = E_0 \eta^k$ after k collisions. Using $\ln x^k = k \ln x$ in

$$\frac{\ln(N/N_0)}{\ln(E/E_0)} = \frac{\ln(\varsigma)}{\ln(\eta)}$$

eliminates the exponent and by rearranging gives the relation

$$N = N_0 \left(\frac{E}{E_0} \right)^{\ln(\varsigma)/\ln(\eta)}$$

as a connection between energy and particle number. This incidentally follows a power law, which is an almost ubiquitous feature observed in cosmic ray physics.

One can interpret the above expression as an integrated spectrum, leading to

$$\frac{dN}{dE} = \frac{N_0}{E_0} \left(\frac{E}{E_0} \right)^\alpha$$

for the differential case with a characteristic spectral index

$$\alpha = \frac{\ln(\zeta)}{\ln(\eta)} - 1$$

constrained by $\ln(\zeta)/\ln(\eta) < 0$ due to $\zeta < 1$ and $\eta > 1$ as implied per the definitions.

The basic case of *Diffusive Shock Acceleration* (DSA) considers shock fronts that propagate with velocity $\beta = v/c$ in a fully ionized gas. Requiring momentum isotropization without significant energy losses on each side of the discontinuity results in $\ln(\zeta)/\ln(\eta) = -1$ and a corresponding spectral dependence $dN/dE \propto E^{-2}$ that is discussed by [18] as well. A slightly steeper index around $\alpha = -2.5$ can be derived when nonlinear effects are accounted for.

Energy gain increasing linearly with β leads this mechanism to be categorized as Fermi type acceleration of first order, whereas the originally proposed formulation scales like β^2 or as second order. Though shocks exceed the local speed of sound in the astrophysical medium, relativistic velocities are typically not achieved. Consequently, ratios of $\beta \ll 1$ mean that lower order processes are much more efficient in reaching high particle energies.

2.2.4 Cosmic Rays

Consisting of charged particles with strictly non-thermal origins, cosmic rays were first detected at high altitudes over a century ago. Since then, they have become a foundational piece in our understanding of astrophysical sources. Although their flux is dominated by protons, other nuclei as heavy as lead can contribute significant portions at high energies as well. Besides this baryonic component, there are also charged leptons adding to the total population. The exact ratios of these constituents contain information about source compositions, though any reconstruction of individual sources is likely impossible. This is a result of cosmic magnetic fields that scramble the directions of charged particles, leading to a largely isotropic distribution. At the same time, it is possible to constrain the size and field parameters of sources based on the energy of cosmic rays. For this purpose, section 2.2.1 provides the so-called Hillas condition. In combination with the characteristic broken power law spectrum, one concludes that most cosmic rays are of galactic origin, except for the highest energies, which require extragalactic sources [4, 6]. Beyond these ranges, there appears to be a sharp drop that agrees with 2.2.2 in case of a GZK cutoff. Both the spectral shape and the extreme energies are also consistent with a slightly modified DSA scenario as described in section 2.2.3 for cosmic rays [10].

2.2.5 Neutrinos

Their weakly interacting nature introduced by section 2.1.2 is precisely what makes neutrinos so interesting. After being produced, they penetrate most obstacles that would be completely opaque to any other messenger particle. This comes at the cost of being notoriously difficult to detect, of course, but opens up the opportunity of measuring otherwise inaccessible processes occurring deep inside astrophysical sources. Several different populations are either known or hypothesized, for example those of solar origin, neutrinos from core-collapse supernovae, stellar remnants or active galaxies that are treated in this work, as well as neutrinos from pion decay implied in section 2.2.2 after GZK photodissociation. Additionally, a primordial neutrino background is expected to exist with a history analogous to that of CMB formation, in which photons decoupled from matter during the recombination epoch. All of these astrophysical and cosmological prospects as well as the previously mentioned flavor oscillations make neutrino astronomy a promising field of research.

2.2.6 Photons

With visual observations being conducted for millenia, photonic signals undoubtedly form the most ancient form of astronomy. Advances in optical instrumentation have driven revolutionary progress over the last centuries, culminating in modern detectors unlocking wavelengths across the entire electromagnetic spectrum. Especially radio and gamma frequencies have the potential of contributing to multimessenger astrophysics, with radio waves having the ability to resolve regions obscured by dust, and gamma photons being closely associated with hadronic processes in a similar manner as neutrinos, for instance.

2.2.7 Gravitational Waves

Setting aside the possibility of gravitons as hypothetical mediating particles, gravitation seems to be a fundamentally continuous phenomenon, in the same way as classical theories like that of electromagnetism by Maxwell. According to Einstein, masses lead to distortions of spacetime that propagate at the speed of light. From this perspective, it readily follows that especially massive systems such as black hole or neutron star binaries emit gravitational waves through their movement. These excitations have an advantage compared to other messengers in that they experience essentially no absorption or scattering by matter. Alongside unimpeded insights into highly energetic merger events, there should also exist a gravitational background radiation containing information about the very early universe.

2.3 Astrophysical Sources

The picture of particle physics building up to multimessenger astronomy will now be realised in the context of plausible astrophysical neutrino sources [10]. In the following section, scenarios for a magnetar as well as an AGN accretion disk are developed.

2.3.1 Magnetars

Neutron stars are stable remnants of massive stellar progenitors that are destroyed in violent core-collapse supernovae after having depleted their fuel reserves. Instead of nuclear fusion, the remaining neutron star is supported against further gravitational contraction by degeneracy pressures. These result from the Pauli exclusion principle that prevents fermions from occupying identical quantum states. While white dwarfs rely primarily on electrons for this mechanism, neutron stars depend on the repulsion among nucleons, placing them among the most dense macroscopic objects in the universe. Due to some angular momentum of the progenitor star usually being conserved in the remnant, the compression of stellar material immediately before a supernova explosion leads to extremely fast rotational periods. In addition to that, conservation of magnetic energy implies large magnetizations as well. Reference [19] discusses this possibility of so-called fossil fields, but argues that strong convective flows during formation or inside the very young neutron star are more likely culprits. These would also remove any previous correlation between the axis of rotation and the field orientation. Because neutron star interiors are assumed to be superconducting fluids, dynamo effects can amplify and sustain any initial magnetic fields [20]. If such a magnetized rotator emits misaligned radio jets, their sweeping motion will be observed as a pulsating radio source, hence the name pulsar. The decay of fields is generally modeled as exponential or according to a power law, but can be assumed to be static for the shorter timescales relevant to the present work [21]. Surrounding young neutron stars are clouds of ejected material, which serve as target fields. Inside this plasma, free charges weaken the otherwise strong fields, allowing synchrotron losses to be neglected.

When extreme magnetic fields in the range of $B = 10^{15}$ G are achieved, the respective neutron star is classified as a magnetar. To fully model these sources, additional parameters are required. Typical neutron star radii are of the order $R = 10^6$ cm with masses of $M = 1.4 M_\odot$ in accordance with the Chandrasekhar limit that defines the maximum stable mass for white dwarfs. From the solar mass $M_\odot = 2 \times 10^{33}$ g follows a moment of inertia $I = 8 \times 10^{44}$ g cm² for our magnetar that has been approximated as a rigid homogenous sphere. Adding to the inaccuracy introduced by discounting any internal structure are the effects of highly relativistic rotation. Due to only using rough estimates anyway, setting $I = 1 \times 10^{45}$ g cm² produces no discernable difference in the final results. Provided by [22] is the minimum period of uniform rotation, beyond which the neutron star loses its structural integrity. Choosing an optimistic value of twice this minimum time $T = 0.3$ ms yields $\omega_0 = 10^4$ s⁻¹ for the initial angular frequency. Lastly, the tilt χ between rotational axis and magnetic field symmetry must be set. As for all previous parameters, the same choice as in [15] is made, with an angle $\chi = 0.95$ in radians.

Concluding this numerical setup is the modeling of the supernova ejecta as a target field for accelerated particles. Assuming this to be a spherical region of homogeneously distributed matter at each time t after formation of the magnetar leads to $n = 3M_{\text{ej}}/(4\pi r_{\text{ej}}^3 m_p)$ as the number density for the case of protons with masses m_p making up all ejected material. From further asserting radial expansion at constant relative velocity β_{ej} one obtains the ejecta radius $r_{\text{ej}} = \beta_{\text{ej}} ct$ as a function of time. With total ejecta masses being similar to that of the progenitor star, values between $10 M_\odot$ and $35 M_\odot$ are possible. Here, the lower bound of $M_{\text{ej}} = 10 M_\odot$ is adopted. With velocities $\beta_{\text{ej}} = 0.1$ of typical supernova shocks, the model is completed.

2.3.2 Spindown

To explain observations of rapidly spinning neutron stars or pulsars, there has to exist some mechanism by which rotational energy is lost. Reference [23] gives a brief overview of possible radiation candidates such as gravitational quadrupolar or higher order electromagnetic moments. Because this work is limited in its scope and concerns itself with the acceleration of electric charges, a pure magnetic dipole approach will be adopted. For more compact and convenient notation, Gaussian units are used.

In an idealized view like [24] of stars as sharply bound and uniformly magnetized spheres, one finds $\mu = R^3 B/2$ for the external magnetic moment. The parameters R and B measure stellar radius and polar magnetic flux density, respectively. In case of a rotating dipole in vacuo,

$$L = \frac{2\mu^2 \omega^4 \sin^2 \chi}{3c^3} \quad (4)$$

is the exact expression for radiant power derived in [25] as a standard reference, where a static angle χ between the dipole field and rotational axis with angular frequency ω is assumed. If a force free limit is applied instead, variational calculations [26] and simulations [27] indicate

$$L = \frac{\mu^2 \omega^4 (1 + \sin^2 \chi)}{c^3} \quad (5)$$

as an appropriate expression of the luminosity. This is more accurate than the previous result, as it has been shown by [28] that the surroundings of a neutron star cannot support a vacuum but must instead be filled with a plasma of charge carriers originating from instabilities at the surface. However, one quickly encounters the problem that $\mathbf{E} \cdot \mathbf{B} = 0$ as a condition of force free magnetospheres prevents particle acceleration. As [29] and [30] discuss, this can be overcome by introducing deviations from such a global solution on local scales.

Spindown is described by an exponential energy decay $E = E_0 \exp(-t/t_{\text{sd}})$ with a characteristic timescale t_{sd} and $\dot{E} = -E/t_{\text{sd}}$ for the time derivative. Assuming all energy is stored in rotational form, the expressions $E = I\omega^2/2$ and $\dot{E} = I\omega\dot{\omega}$ are also valid with I as the neutron star moment of inertia. Equations (4) and (5) can be generalized as $L = K\omega^4$ by using a coefficient K containing all other information except the dipolar ω^4 dependence. Identifying this with the energy loss via $\dot{E} = -L$ and evaluating at $t = 0$ yields $L_0 = K\omega_0^4$ as well as $\dot{E}_0 = -I\omega_0^2/2t_{\text{sd}}$ for an expression of $t_{\text{sd}} = I/2K\omega_0^2$ as the spindown time. It further follows for any t that $I\dot{\omega} = -K\omega^3$ must hold. This is a special case of the power law differential equation $\dot{\omega} \propto \omega^n$ with $n = 3$ as the so-called braking index typical of a rotating magnetic dipole. For comparison, one would find $n = 5$ in case of a quadrupole, indicating that n is characteristic of the specific energy loss mechanism involved. After separating variables and integrating, one obtains $\omega = \omega_0(1 + t/t_{\text{sd}})^{-1/2}$ for the frequency as a function of time.

Another important concept in neutron star environments is the so-called light cylinder. Defined via $R_{\text{lc}} = c/\omega$ as the radius, it describes the boundary beyond which magnetic field lines are

unable to corotate with the central body without exceeding the speed of light. Thanks to the resulting lag, magnetic fields are open, providing a potential acceleration mechanism.

With an open field magnetic flux $\psi = \mu/R_{lc}$ follows $\phi = \psi/R_{lc}$ for the potential drop. From this, a particle with charge e reaches energies of $E^M = \eta e\phi$ where η measures the acceleration efficiency. Expanding these terms and including the dependence on time,

$$E^M(t) = \frac{\eta e B R^3 \omega_0^2}{2c^2(1 + t/t_{sd})} \quad (6)$$

states this explicitly. The superscript M denotes a monochromatic energy distribution.

2.3.3 Active Galactic Nuclei

As the bright centers observed in some galaxies, such compact cores are emitters of extreme energies, making them prime candidates for UHECR acceleration. It is accepted that AGN are driven by SMBH central engines. These black holes are assumed to be of Kerr type, giving them a spin and an according angular momentum [31]. Through interactions of infalling material and magnetic fields, this rotational energy can be extracted to form highly relativistic jets [32]. In the plane of rotation surrounding the central mass, one usually finds an accretion disk emitting lumious thermal radiation, a thorough review of which is given by [33]. The SMBH is enveloped by a bubble of highly magnetized hot plasma, the so-called corona region. Included in [34] is a brief overview of the unified AGN model that supposes a generally similar structure for all active galactic cores. In this view, distinct AGN types are differentiated by their radio emissivity and total luminosity, as well as the relative orientation in the direction of an observer. The last feature predicts the measured effects of broad and narrow line regions or the obstruction by a dusty torus that is situated around the outer accretion disk. Potential sources of high energy neutrinos in this complex environment are discussed by [35]. For the work at hand, a general DSA mechanism is assumed, which injects energetic particles onto a static accretion disk as the proton target. The responsible shocks have several possible origins, such as the corona or the disk itself. Other options are jet shocks that travel towards the inner region or starburst events in the surrounding galaxy as tested in [36]. One more critical assumption is that of vanishing magnetic fields inside the AGN disk, which is necessary to neglect synchrotron losses.

The typical SMBH has masses around $10^8 M_\odot$ with 2 AU as a Schwarzschild radius. While jets can reach enormous scales of multiple 100 kpc with terminal bow shocks at Mpc distances from the core, itself contained within 1 pc sizes, accretion disks extend to radii of $R = 10$ mpc with heights around $h = 100$ AU being plausible. Rough densities of $n = 10^{15} \text{ cm}^{-3}$ may be assumed on average, with a more detailed description provided in the following paragraphs.

2.3.4 Accretion Disks

Diffusely distributed material in orbit around a central massive object naturally produces flat structures. This is a consequence of gravitational forces being compensated in the radial plane

by rotational effects while matter is relatively free to collapse in the axial direction. Compression and friction during inward spiraling heat the disk, thereby emitting intense thermal radiation.

Settings where these phenomena likely occur are protoplanetary disks surrounding newly formed stars or accretion flows on a SMBH inside the galactic core region, among others. The following describes some related effects that are for example discussed by [18] as well.

Hydrostatic Equilibrium

In Newtonian physics, the gravitational force at distance R from a mass M is given as

$$F = \frac{GMm}{R^2} \quad (7)$$

for particles with masses m orbiting the central object. The resulting acceleration is therefore of magnitude $g = GM/R^2$ with vertical component $\ddot{z} = g \sin(\vartheta)$ and ϑ as the angular elevation. In case of $\vartheta \ll \pi/2$ one can approximate $\sin(\vartheta) = z/R$ to obtain

$$\ddot{z} = \frac{GMz}{R^3}$$

which is related to pressure p and density ρ via $dp/dz = -\rho\ddot{z}$ for a stable equilibrium to exist. Using the speed of sound $u^2 = dp/d\rho$ allows reformulation to

$$\frac{d\rho}{dz} = -\rho \frac{GMz}{u^2 R^3}$$

and $\rho = \rho_0 \exp(-z^2/2h^2)$ after integration. According to this result, the disk density follows a centered Gaussian distribution with height parameter h defined via

$$h^2 = \frac{u^2 R^3}{GM}$$

as the standard deviation. Assuming $M \gg m$ and circular Keplerian orbits, expression (7) equals the acting centripetal force, leading to $v^2 = GM/R$ for the orbital velocity. One is then able to write $h^2 = u^2 R^2 / v^2$ and from the necessary condition $h \ll R$ for the small angle approximation follows $u \ll v$ or that orbital velocities must greatly exceed the speed of sound specific to the medium. This special case is called a thin disk and can further be extended to slim or even thick types of accretion structures.

Luminosity Limit

Any luminous object radiating with spherical symmetry exerts a pressure

$$P = \frac{L}{4\pi R^2 c}$$

as a function of luminosity L at distance R from the source. Suppose a gaseous cloud containing particles with masses m falling towards the same bright central mass M due to gravitational attraction. During this process, each particle experiences $F = \kappa m P$ as an opposing radiative force, where the opacity κ measures cross section per unit mass.

Balancing of (7) and rearranging leads to the Eddington limit

$$L = \frac{4\pi GMc}{\kappa} \quad (8)$$

on the luminosity beyond which additional matter is immediately blown away from the central object. By assuming that infalling material consists exclusively of ionized hydrogen, one can approximate $\kappa = m/\sigma$ with proton mass m and Thomson cross section σ from electron scattering. Though originally applied in the context of stellar structures, this approach can also be used to describe accretion disks. If a compact object increases its mass with rate \dot{M} due to accreting matter, some of the corresponding gravitational potential may be converted to radiation. In terms of rest energy, a luminosity $L = \eta \dot{M} c^2$ is obtained where η denotes the efficiency of this mechanism. With (8) one finds an analogous steady state limit

$$\dot{M} = \frac{4\pi GM}{\eta c \kappa}$$

for the accretion rate, enforced by continuous balancing of radiation pressure and gravitational forces as an intrinsic feedback process.

3 Methods

Building on a physical background, this chapter first introduces generally applicable methods for the translation of an injected proton distribution to a hadronic spectrum, which then decays to create neutrinos. Subsequently, the injection spectra are described for the previously specified astrophysical settings. To start with, a general case $a \rightarrow b$ is defined for the reaction. Given a spectrum dN_a/dE_a that describes the number N_a of particles a per E_a energy interval, as well as the spectral distribution $F_{a \rightarrow b}$ for the probability that particles b are produced by a singular interaction, one can solve the folding integral

$$\frac{dN_b}{dE_b}(E_b) = \int_{\hat{E}_a}^{\hat{E}_a} dE_a \frac{dN_a}{dE_a}(E_a) F_{a \rightarrow b}(E_b, E_a) \quad (9)$$

to obtain their numbers N_b with respect to E_b energies. From this formulation, it is clear that both distributions and spectra should be assumed to depend on energy, with other arguments such as the time t being allowed as well. Additionally, integration bounds $\check{E}_a \leq \hat{E}_a$ must always be specified, which are usually dictated by kinematic constraints.

To implement and compute all following parametrizations, the *Python* programming language and its library *Numpy* are used. Graphical results are created via the *Matplotlib* package.¹

3.1 Cross Sections

By defining an effective area perpendicular to the momentum vectors of projectiles and targets, cross sections as described by section 2.1.4 measure probabilities of collision processes in particle physics and are therefore required for the calculation of spectral distributions.

3.1.1 Scattering

To model total cross sections in hadron-proton scattering, this work uses the formula

$$\sigma_{hp} = H_h \ln^2(s/s_h) + P_h + R_h^1(s_h/s)^{\eta_1} + R_h^2(s_h/s)^{\eta_2} \quad (10)$$

¹ In service of reproducibility, all implementations can be viewed in [this](#) repository.

as given in [37] for a universal analytic parametrization of the corresponding amplitudes.

All adjustable parameters are listed in table 1 together with relevant meson lifetimes for cooling. In this approach, the variable M relates to $H = \pi(\hbar c/M)^2$ and $s_h = (m_h + m_p + M)^2$ as an effective mass. Coefficients in (10) are named after Heisenberg, Pomeranchuk and Regge, respectively, and have some qualitative motivation, though the formula itself is primarily a quantitative result.

TABLE 1: Fits to the total inclusive scattering cross sections in hadron-proton collisions. Parameters are taken from [37] with $M = 2.121$ GeV for $H = 0.272$ mb as the rate of growth. Both $\eta_1 = 0.447$ and $\eta_2 = 0.5486$ are dimensionless exponents. Decay times τ_h and rest masses m_h can be found in the particle listings [16] where the latter are given in natural units.

h	P_h / mb	R_h^1 / mb	R_h^2 / mb	τ_h / ns	m_h / GeV	s_h / GeV ²
p	34.41	13.07	7.39		0.938	15.98
π	18.75	9.56	1.767	26.03	0.140	10.23
K	16.36	4.29	3.408	12.38	0.494	12.62

Assuming a quasi universal ratio \mathcal{R} between elastic and total hadron cross sections, one obtains the inelastic cross section $\sigma_{\text{inel}} = (1 - \mathcal{R})\sigma_{\text{tot}}$ from $\sigma_{\text{el}} = \mathcal{R}\sigma_{\text{tot}}$ and $\sigma_{\text{el}} + \sigma_{\text{inel}} = \sigma_{\text{tot}}$ as a unitarity condition. Provided in [38] is the model independent parametrization

$$\mathcal{R}(s) = \frac{\sigma_{\text{el}}(s)}{\sigma_{\text{tot}}(s)} = \mathcal{A} \tanh(\gamma_1 - \gamma_2 \ln(s) + \gamma_3 \ln^2(s)) \quad (11)$$

with a constant asymptote \mathcal{A} at very high energies. Coefficients are given in table 2 for different physical settings. Both equations (10) and (11) use units of GeV² for the s variables. Combining these, figure 1 depicts the scaling of inelastic cross sections with energy for different hadrons.

TABLE 2: Almost model independent ratio of hadronic elastic and total scattering cross sections. Factors γ are taken from [38] for varying \mathcal{A} asymptotes.

\mathcal{A}	γ_1	γ_2	γ_3
1/2	0.466	0.0259	0.00177
1	0.2204	0.0111	0.00076

Reference [39] tests the asymptotic rise $\sigma(s) \propto \ln^2(s)$ derived in [40] as a theoretical upper bound and concludes that it is somewhat exceeded. Additionally, a ratio $\mathcal{A} = 1/3$ due to diffraction as opposed to the black disc limit $\mathcal{A} = 1/2$ from optical theorem predictions is suggested [39]. Because parameters are only available in the latter case, all calculations of \mathcal{R} use (11) as defined

by an asymptote $\mathcal{A} = 1/2$ for this work. Data matching $\mathcal{A} = 1/3$ then imply that $\sigma_{\text{inel}}(s)$ is slightly underestimated, though this is unlikely to significantly influence the overall results.

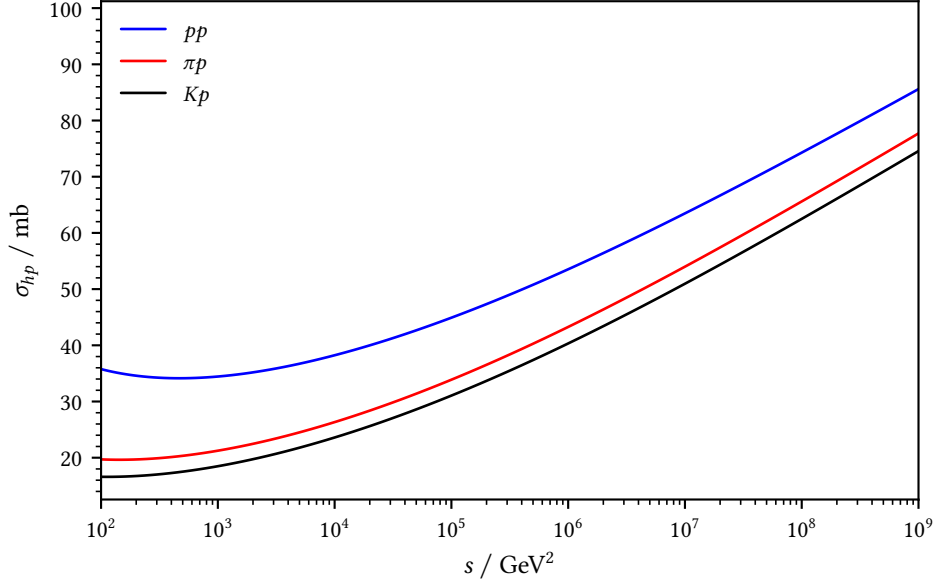


FIGURE 1: Inelastic cross sections σ_{hp} for hadron-proton scattering according to the parametrizations (10) and (11) reproducing an asymptotic $\ln^2(s)$ scaling.

3.1.2 Production

For charm quark production in proton-air collisions, reference [41] gives

$$x_F \frac{d\sigma}{dx_F}(x_F, E_p) = ax_F^b (1 - x_F^m)^n$$

as the parametrized differential cross section with components

$$a = a_1 \ln(E_p) - a_2 \quad b = b_1 - b_2 \ln(E_p) \quad n = n_1 - n_2 \ln(E_p)$$

for which table 3 lists all necessary constants. Here, proton energies E_p are defined as viewed by air nuclei at rest, while the Feynman scaling variable $x_F = p_c/p_s$ specifies magnitude ratios of produced charm quark longitudinal momentum to all available momentum in center mass coordinates of the colliding particles. Application of section 2.1.3 shows that this approximately fulfills $x_F = x_c$ where $x_c = E_c/E_p$ in the relevant energy ranges. It should be noted that for the values table 3 provides, the coefficient $n_0 = 0.075$ from table 1 in [41] for the lower energy regime is set to $n_0 = 7.5$ instead, because the parametrization breaks down otherwise. Further testing reveals another problem with the 10^4 GeV to 10^8 GeV region, in that energies around 26 TeV or lower yield negative differential cross sections. Considering other approximations made in

this work, it is therefore decided that an extrapolation from the 10^8 GeV to 10^{11} GeV case to all energies can be done without producing unreasonably large errors.

TABLE 3: Parametrization of the inclusive charm quark production differential cross section. Coefficients are calculated from [41] to write E_p in units of GeV without needing redundant conversion steps. The exponent $m = 1.2$ is a constant at all energies. For the application at hand, energy ranges beyond the given validity intervals are used as mentioned in the text.

E_p / GeV	a_1 / μb	a_2 / μb	b_1	b_2	n_1	n_2
$10^4 - 10^8$	826	8411	0.197	0.016	8.486	0.107
$10^8 - 10^{11}$	403	2002	0.237	0.023	7.639	0.102

Borrowing from [42] among others, linear scaling with nucleon number is assumed, giving

$$\frac{d\sigma}{dx_c}(x_c, E_p) = \tilde{A}^{-1} \frac{d\sigma}{dx_F}(x_c, E_p)$$

for inclusive charm production in proton-proton collisions. Approximating air as a gas mixture of roughly 75 % nitrogen and 25 % oxygen, one finds $A = 14.5$ for this factor. By integrating the charmed hadron cross section defined below and comparing to experimental data in [43] for the charm mesons considered in this work, one finds that calculated values exceed measurements by a factor 22.32 ± 2.34 on average, yielding $\tilde{A} = 323.64$ as a modification to enforce compatibility with observations. One problem of this approach is that [43] provides values at $\sqrt{s} = 13$ TeV or roughly $E_p = 9$ PeV only, so that deviations at different energies are not accounted for. Similar to earlier reasoning, the resulting inaccuracy is deemed acceptable.

Translation of charm quarks to charmed hadrons is achieved with an integral

$$\frac{d\tilde{\sigma}}{dx_h}(x_h, E_p) = \int_{x_h}^1 dz z^{-1} \frac{d\sigma}{dx_c}(x_c, E_p) D_c^h(z) \quad (12)$$

where $z = E_h/E_c$ and $x_h = E_h/E_p$ as well as $x_c = x_h/z$ are fractional energies. Limits for the integration follow from a basic inequality $E_h \leq E_c \leq E_p$ to incorporate kinematic constraints. Furthermore, the probability of observing any final state h originating from a c quark is encoded in a *Fragmentation Function* (FF) $D_c^h(z)$ dependent on the fraction of hadron to charm energy. Reference [44] addresses the connection between this concept and that of a *Parton Distribution Function* (PDF) among other things. While a PDF represents the probability density of finding a parton with given momentum inside a colorless particle, probabilities for color neutral-states existing in individual partons are given by the appropriate FF instead. The partons described here are either quarks or gluons, which sections 2.1.1 and 2.1.2 describe more closely.

By fitting to existing data or perturbative calculations, models can extrapolate to low momentum

fractions that have not yet been probed experimentally. This procedure has lead [45] to obtain

$$D_c^h(z) = \frac{N_h z(1-z)^2}{((1-z)^2 + \epsilon_h z)^2} \quad (13)$$

with parameters from e^+e^- data in table 4 as the charm hadron FF used throughout this work. It is important to note that such functions are invariant under charge conjugation, so that there is no differentiation between quark to particle or antiquark to antiparticle processes.

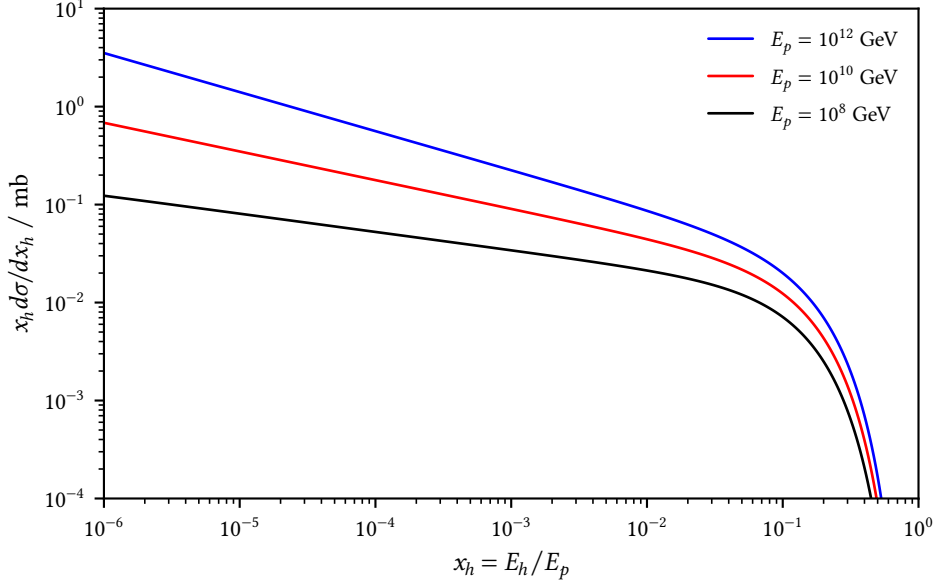


FIGURE 2: Inclusive differential cross sections for $pp \rightarrow D^0 X$ production at different proton energies E_p according to the (14) parametrization.

To account for kinematic constraints, one final modifier has to be included at this point. Because collisions must provide enough energy for particle formation, charmed hadron energies cannot be lower than their rest masses, leading to $E_h \geq m_h$ as a natural condition. With table 4 listing mass parameters, a cutoff similar to that in [46] is introduced, rewriting (12) to

$$\frac{d\sigma}{dx_h}(x_h, E_p) = \frac{d\tilde{\sigma}}{dx_h}(x_h, E_p) \left(1 - \frac{m_h}{x_h E_p}\right)^{1/2} \quad (14)$$

where $E_h = x_h E_p$ ensures physical kinematics are respected. It turns out that this expression is integrable, whereas the unmodified version (14) is not. Shown in figure 2 is the D^0 differential cross section for different incident proton energies and fixed protons as targets. Comparing this to figure 7 in [15] indicates similar shapes, though our parametrizations result in less flat distributions at low x_h values.

3.2 Spectral Distributions

Constructing spectra dN_h/dE_h from proton injection requires folding of $F_{p \rightarrow h}$ as the hadronic distribution for a single pp interaction with the number of protons per energy interval given by the function dN_p/dE_p obtained from source specific modelling. An analogous approach can be applied to compute neutrino spectra dN_ν/dE_ν from dN_h/dE_h via distributions $F_{h \rightarrow \nu}$ formulated according to the involved decay modes. Equation (9) describes exactly this, with the following section providing all required distributions.

3.2.1 Charm

Spectral distributions for charmed hadron production are calculated according to [15] through

$$F_{p \rightarrow h}(E_h, E_p) = E_p^{-1} \sigma_{pp}^{-1}(E_p) \frac{d\sigma}{dx_h}(x_h, E_p)$$

with $E_h = x_h E_p$ translating between variables. This can be understood as weighting (14) against the energies and inelastic cross section of protons scattered as described in section 3.1.1 to yield hadron numbers per unit energy.

To find neutrino spectra from charmed hadrons, the same approach as in [47] is used, which assumes an effective energy distribution approximated by three body decays for the semileptonic channel to a less massive pseudoscalar meson. By neglecting lepton masses, one obtains

$$\tilde{F}_{h \rightarrow \nu}(y) = D_h^{-1} \left(6b_h a_h^2 - 4a_h^3 - 12\lambda_h^2 a_h + 12\lambda_h^2 y - 6b_h y^2 + 4y^3 + 12\lambda_h^2 \ln((1-y)/\lambda_h) \right)$$

as a distribution with $y = E_\nu/E_h$ and $F_{h \rightarrow \nu}(E_\nu, E_h) = \mathcal{F}_h \tilde{F}_{h \rightarrow \nu}(y)/E_h$ for conversion.

Hadron specific coefficients for this equation are defined with the parameter $\lambda_h = \tilde{s}_h/m_h^2$ as

$$a_h = 1 - \lambda_h \quad b_h = 1 - 2\lambda_h \quad D_h = 1 - 8\lambda_h - 12\lambda_h^2 \ln(\lambda_h) + 8\lambda_h^3 - \lambda_h^4$$

where both s_h and m_h are listed in table 4 for all included charmed hadrons. The assumption of three body decays like $D^+ \rightarrow \bar{K}^0 e^+ \nu_e$ can be justified by consulting [16] for information on the relevant particles and comparing branching ratios, which indicate that purely leptonic modes are strongly suppressed. Hadronic channels such as $D^+ \rightarrow \pi^+ \pi^0$ or $D^+ \rightarrow K^- \pi^+ \pi^+$ are either very improbable as well or occur at significant rates but do not contribute many high-energy neutrinos due to pions and kaons being subject to further cooling before decaying to leptons. By the same logic, secondary muon decay is neglected when determining the neutrino spectrum.

TABLE 4: Coefficients for charm hadron production, cooling and decay to neutrinos.

All parameters ϵ_h are taken from leading order QCD fits via the FF as defined and described in [45] with normalizations N_h given by [15] to rescale the integration of (13) over $[0,1]$ to approximately match the fractions f_h provided in [48] from measurements. Effective masses $\sqrt{s_h}$ and branching fractions F_h are determined by [49] and [47] from fitting decay rates. Mean lifetimes τ_h and masses m_h are adopted from [16] in the particle listings. Mass type quantities use natural units.

h	N_h	ϵ_h	τ_h / fs	F_h	$\sqrt{s_h}$ / GeV	m_h / GeV
D^0	0.577	0.101	410	0.067	0.67	1.86
D^+	0.238	0.104	1033	0.176	0.63	1.87
D_s^+	0.0327	0.0322	501	0.065	0.84	1.97
Λ_c^+	0.0067	0.00418	203	0.045	1.27	2.29

3.2.2 Pions & Kaons

By parametrizing event generator results, a neutral pion production spectrum of the form

$$\tilde{F}_\pi(x_\pi, E_p) = 4\alpha B x_\pi^{\alpha-1} \left(\frac{1 - x_\pi^\alpha}{1 + r x_\pi^\alpha (1 - x_\pi^\alpha)} \right)^4 \left((1 - x_\pi^\alpha)^{-1} + \frac{r(1 - 2x_\pi^\alpha)}{1 + r x_\pi^\alpha (1 - x_\pi^\alpha)} \right) \left(1 - \frac{m_\pi}{x_\pi E_p} \right)^{1/2}$$

is found in [46] with $m_\pi = 0.135$ GeV [16] translated to natural units and parameters

$$B = \tilde{B} + C \quad \alpha = \frac{\tilde{\alpha}}{\sqrt{C}} \quad r = \frac{\tilde{r}}{\sqrt{C}}$$

where a low energy cutoff is enforced via $E_\pi = x_\pi E_p$ in the mass term. From

$$C = c_1 - c_2 \ln(E_p) + c_3 \ln^2(E_p)$$

results a dependence on projectile energy for the shape of this distribution.

Coefficients are specified in table 5 and recalculated for E_p in GeV instead of TeV units. Under the assumption of a π^0 cross section approximately equal to the π^\pm average and with identical spectra for charged pions, it follows that $F_\pi = \tilde{F}_\pi/E_p$ should describe pion production regardless of charge reasonably well for the purpose of this work.

TABLE 5: Parametrized spectral distribution for neutral pion production. Factors are taken from [46] and converted to write E_p in GeV for the unitless c_k coefficients.

\tilde{B}	$\tilde{\alpha}$	\tilde{r}	c_1	c_2	c_3
0.25	0.98	2.6	1.515	0.206	0.075

For a convenient formulation of kaon production, references [50] and [51] indicate a constant ratio π/K at moderately high energies. Similar fractions are retrieved from multiplicities given in [52] and lead to $F_K/F_\pi = 0.12$ as a simplifying assumption, the validity of which cannot be guaranteed for the application at hand. Calculations of kaon spectra still employ this approach but are subject to considerable reservations as a result, because fixed ratios to pion spectra are unlikely to be universal. Other than this factor, the pion mass is replaced with that of kaons for a correct cutoff in the above expression.

Decays of pions and kaons to neutrinos are approximated via the $h \rightarrow \mu^+ \nu_\mu$ two body channel with branching fractions of $\mathcal{F}_\pi = 99.99\%$ and $\mathcal{F}_K = 63.56\%$ given in the [16] particle listings. By decaying, muons produced in these processes can significantly impact the neutrino spectrum. Results from [15] suggest that this is particularly relevant for pions. Muonic three body decays of type $\mu^- \rightarrow e^- \bar{\nu}_e \nu_\mu$ as well as cooling factors depend on the polarization of participating leptons due to the nature of weak force coupling. This complicates computations and is thus omitted in service of restricting the present work to a manageable scope, though it should be remembered as an important caveat for the final results.

The remaining two body decays of ultrarelativistic hadrons h to leptons l obey a distribution

$$F_{h \rightarrow l}(E_l, E_h) = \mathcal{F}_h E_h^{-1} (1 - \lambda_h)^{-1}$$

with $m_\nu = 0$ and $m_\mu = 0.106$ GeV [16] as well as $\lambda_h = m_\mu^2/m_h^2$ as a parameter. This formula is the same whether $l = \nu$ or $l = \mu$ because there is one muon for each neutrino. In addition, kinematic considerations lead to $E_\mu/E_h > \lambda_h$ and $E_\nu/E_h < 1 - \lambda_h$ for bounds $E_\mu < E_h < E_\mu/\lambda_h$ in case of muons or corresponding limits $E_\nu/(1 - \lambda_h) < E_h < E_p$ when considering neutrinos, which are required by (9) for integration.

3.3 Computation

Taking into account previous deliberations, this section now combines these with the contents of chapter 2 to give explicit steps for calculating the desired results.

3.3.1 Injection

Modeling proton spectra of young magnetars described in section 2.3.1 starts with an idealized charge density $\rho = \omega B_{\text{ns}}/(2\pi c)$ derived from [28] and leads to $n = \rho/e$ for the number of charge carriers. Integrating over the so-called polar caps defined by a radius $R_{\text{pc}} = R_{\text{ns}}\sqrt{R_{\text{ns}}/R_{\text{lc}}}$ from which open field lines originate, and taking E^M according to (6) as a monochromatic energy for all times t results in a time-derivative delta-functional spectrum

$$\frac{d\dot{N}_p}{dE_p}(t, E_p) = \frac{B_{\text{ns}}R_{\text{ns}}^3\omega_0^2}{ec(1 + t/t_{\text{sd}})}\delta(E_p - E^M(t)) \quad (15)$$

that is compatible with a $dN_p/dE_p \propto E_p^{-1}$ power law.

For the AGN setting, a more general DSA scenario like in section 2.2.3 is assumed, yielding

$$\frac{dN_p}{dE_p} = S E_p^{-2}$$

with S for an arbitrary unitless normalization factor that does not need to be specified further, as this work is interested in relative neutrino contributions instead of absolute predictions.

3.3.2 Production & Decay

Spectra of hadrons and neutrinos are generally computed as in (9) via folding, though for the hadronic spectrum, a cooling factor (1) from section 2.1.5 as well as an effective optical depth are included via multiplication. With the ratio of source size d and mean free path λ defining this optical depth $f = d/\lambda$ as a dimensionless factor, it represents a measure of proton-proton interactions taking place. Accordingly, section 2.1.5 gives $\lambda = (\kappa_{pp}\sigma_{pp}n)^{-1}$ and $d = r_{\text{ej}}$ for a magnetar or $d = h/\sin\alpha$ in an AGN scenario. While r_{ej} adds an explicit time-dependence to the implicit evolution implied by $E^M(t)$ proton energies, the AGN instead depends on an angle α measuring the direction of incidence relative to the normal vector of the accretion disk plane. The height parameter defined in section 2.3.3 varies with radius and characterizes diffuse density distributions. In contrast to this, the highly simplified case considered here instead assumes a sharply bound disk of constant height. Cross sections and spectra are taken as presented in sections 3.1 and 3.2 with charmed hadron scattering cross sections being approximated to that of kaons.

3.4 Implementation

In order to calculate neutrino spectra from hadronic distributions, several integrals have to be computed. Discretizing this task allows the general case

$$F(x, y) = \int_{z_-}^{z_+} dz G(x, z) H(z, y)$$

to be rewritten as a Riemann sum. Assuming G and H are integrable over a given interval,

$$F_{ij} = \sum_k D_{kk} G_{ik} H_{kj}$$

converges to the exact solution for sufficiently small steps. Transforming variables

$$x \rightarrow x_i \quad y \rightarrow y_j \quad z \rightarrow z_k$$

and defining $D_{kk} = z_{k+1} - z_k$ leads to the above notation. It is easily shown how this expression in terms of indices translates to the product of corresponding matrices

$$F = GDH$$

as an equivalent formulation. Here the output $\mathbf{F} \in \mathbb{R}^{m \times n}$ is obtained from the inputs $\mathbf{G} \in \mathbb{R}^{m \times l}$ and $\mathbf{H} \in \mathbb{R}^{l \times n}$ as well as the square matrix $\mathbf{D} \in \mathbb{R}^{l \times l}$ that encodes all step sizes on its diagonal. These results enable a quick and efficient implementation of the required calculations as program code, where array arithmetic operations can greatly increase execution speed.²

Logarithmic spacing can lead to better accuracy and fewer steps...

² In service of reproducibility, all implementations can be viewed in [this](#) repository.

4 Results

Presented in this chapter are the results obtained by applying the previously described methods. Due to uncertain normalization factors, all values are given with respect to the maximum charm component in terms of flux $\dot{\phi}_\nu$ or fluence ϕ_ν as physical quantities. By its definition,

$$\dot{\phi}_\nu = \frac{d\dot{N}_\nu/dE_\nu}{4\pi d^2}, \quad (16)$$

the flux counts neutrinos per energy, time and area. Equation (16) derives from evenly spreading all spectral intensity over a spherical surface with radius equal to the distance d from a single source. Integrating over time yields the fluence,

$$\phi_\nu = \frac{dN_\nu/dE_\nu}{4\pi d^2}, \quad (17)$$

which measures neutrino numbers per energy and area instead. Because d is a constant, forming ratios of $\dot{\phi}_\nu$ or ϕ_ν eliminates it. Accordingly, the following results are distance independent.

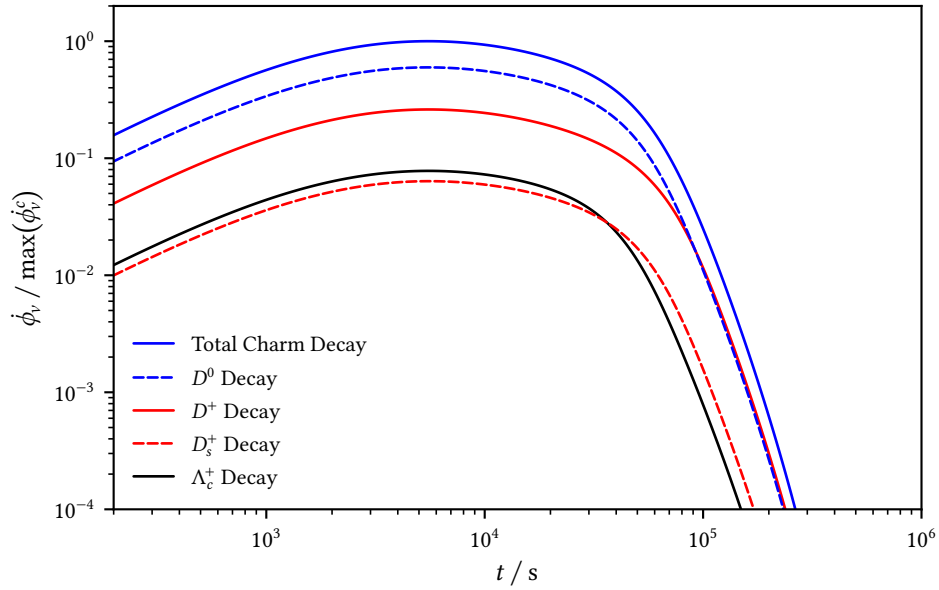


FIGURE 3: Comparison of individual charmed hadron contributions to the total charm neutrino flux at $E_\nu = 10^9$ GeV from a newborn magnetar, including optical depth.

4 Results

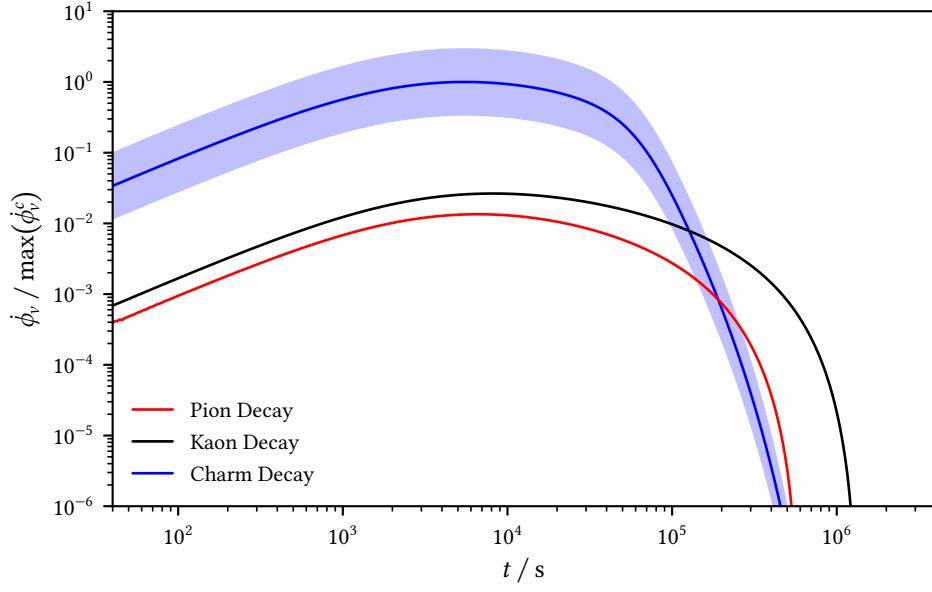


FIGURE 4: Effective neutrino light curves normalized to the maximum charm decay flux at $E_\nu = 10^9$ GeV from a newborn magnetar, including optical depth.

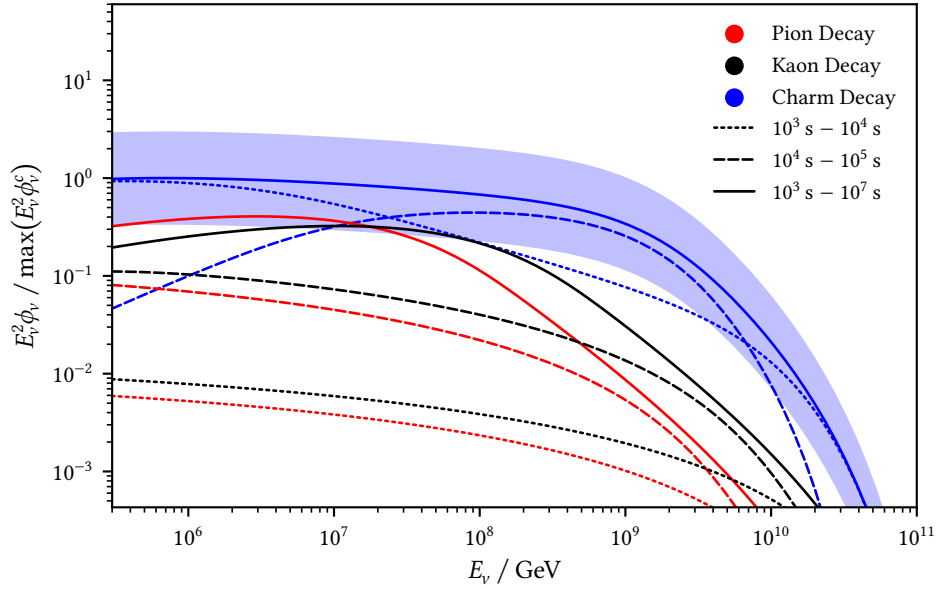


FIGURE 5: Expected neutrino fluence weighted by the charm contribution from a young magnetar for different time intervals after formation, including optical depth.

As mentioned earlier, neutrinos are not distinguished by flavor, but by the particle decay from which they originate. Model parameters use the numerical values that section 3.3 provides.

4 Results

Shown in figure 3 is the temporal evolution of charmed hadron contributions to the total charm component at $E_\nu = 10^9$ GeV originating from a young magnetar. Decays of D^0 constitute most of the charmed neutrinos, with D^+ adding significant amounts as well, especially at later times. Both D_s^+ and Λ_c^+ are roughly the same, each contributing around 10 % to the combined flux. This is in line with cross sections calculated via (14) or measured by [43] as well as the respective branching fractions listed in table 4 for effective three body decays to neutrinos.

Similarly, figure 4 presents light curves for pions and kaons next to the total charm contribution, restricted to $E_\nu = 10^9$ GeV neutrinos. As in [15] from QCD calculations, a factor of $1/3 - 3$ is adopted for the charmed hadron uncertainty and marked with a shaded blue band. Decays of kaons generally contribute more than pions at this energy, with neutrinos from charm exceeding both by more than an order of magnitude until about $t = 10^5$ s after magnetar formation.

In order to evaluate the significance of different time periods, figure 5 depicts integration results over varying intervals for pion, kaon and charm fluence. Contrary to expectations, charmed hadron decays are dominant at all energies by as much as one order of magnitude. Comparing figures 4 and 5 with the corresponding plots in [15] reveals further inconsistencies. Notably, light curves in figure 4 have relatively flat slopes at earlier times, and the charm neutrino fluence in figure 5 shows no decrease towards lower energies. Testing different potential error sources indicates that the optical depth \mathcal{O} is most likely responsible for these discrepancies. Inserting proportionalities of ejecta density $n_{\text{ej}} \propto t^{-3}$ and radius $r_{\text{ej}} \propto t$ into (2) while assuming σ_{pp} to be constant leads to an approximate $\mathcal{O} \propto t^{-2}$ dependence and results in neutrino numbers being distorted significantly towards larger values at earlier times. To verify this finding, calculations are repeated under omission of the optical depth.

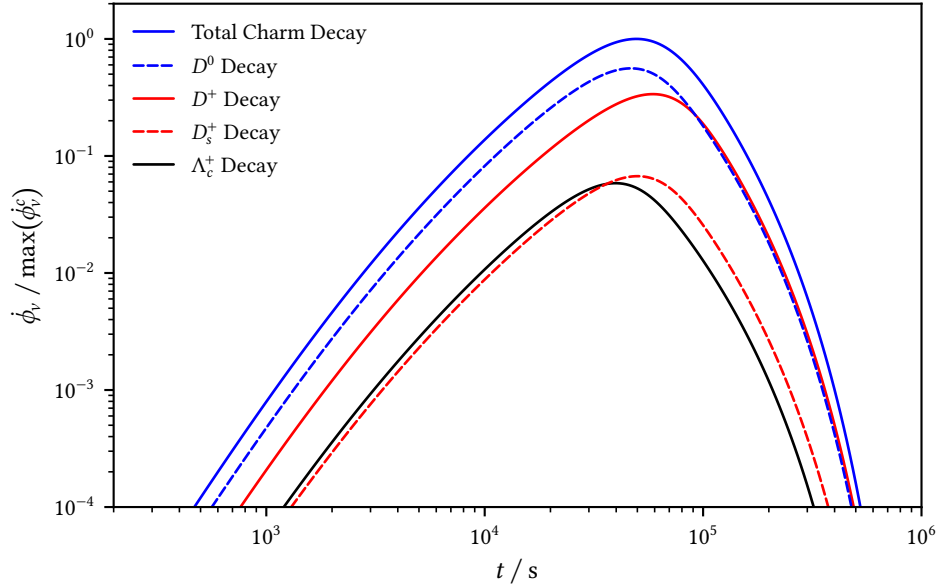


FIGURE 6: Comparison of individual charmed hadron contributions to the total charm neutrino flux at $E_\nu = 10^9$ GeV from a newborn magnetar, excluding optical depth.

4 Results

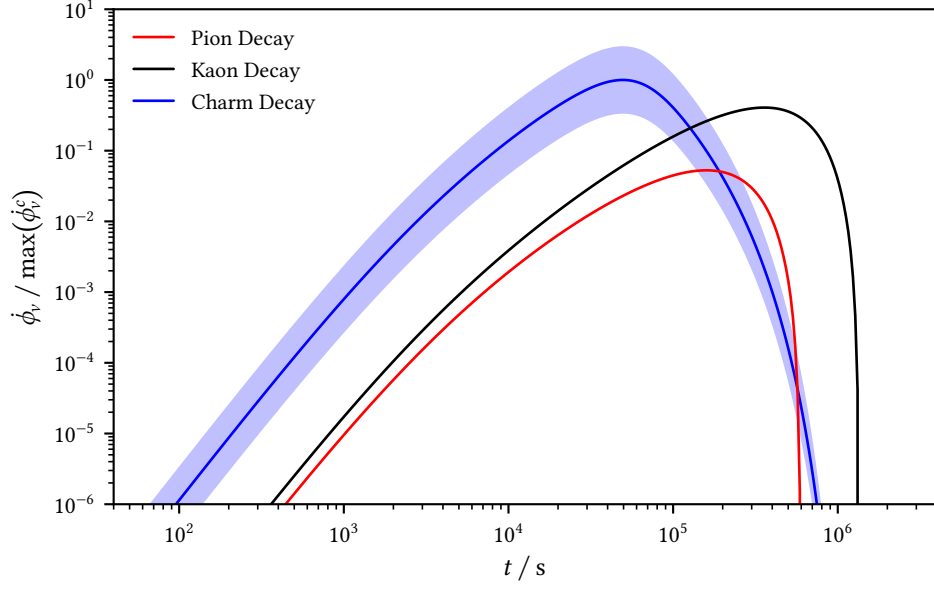


FIGURE 7: Effective neutrino light curves normalized to the maximum charm decay flux at $E_\nu = 10^9$ GeV from a newborn magnetar, excluding optical depth.

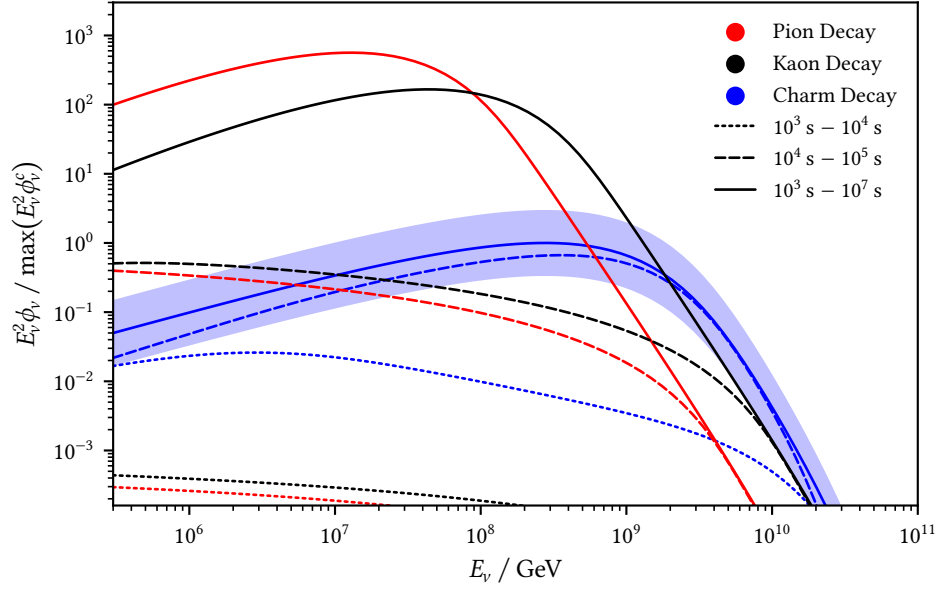


FIGURE 8: Expected neutrino fluence weighted by the charm contribution from a young magnetar for different time intervals after formation, excluding optical depth.

4 Results

As suspected, these results more closely match those in [15]. Starting with the comparison of charmed hadrons, figure 6 agrees with the previous statements regarding D^0 and D^+ dominating over D_s^+ and Λ_c^+ decays. By excluding the optical depth, one can reveal additional information via the identification of comparatively narrow peaks. Their relative positions are consistent with the different mean lifetimes that table 4 lists, an observation which is not accessible from figure 3 due to flux curves resembling broad plateaus rather than clearly defined extrema. Due to shorter decay times resulting in vanishing cooling effects (1) at higher energies, curves are shifted to reproduce slight offsets in charmed hadron contribution.

Again comparing [15] to figures 7 and 8 indicates improved agreement, with distribution shapes that are roughly similar in both cases. Because of differences in the approaches, some deviation is to be expected. Reference [15] uses event generator results to model pion and kaon cross sections, as well as QCD calculations for the charm component, while this thesis collects various parametrizations from the literature for semianalytical computations instead. Especially the almost identical shapes of pion and kaon light curves in figure 7 are most likely a consequence of the simplifying assumption that their spectral distributions are linearly proportional except for a cutoff determined from their rest masses. Despite this, neutrino fluxes from pion or kaon decay individually fit their counterparts in [15] fairly well when the contribution from muons is ignored, and their respective maxima are within acceptable margins compared to the charmed hadron curves in figure 7 and reference [15].

There are, however, certain disagreements that are unlikely to arise purely from variations in the described methodologies. To begin with, reference [15] provides $E^M = 1.3 \times 10^{13}$ GeV as an initial value for the energy of injected protons, which disagrees with inserting the same default parameters into (6) to find $E^M = 1.7 \times 10^{12}$ GeV instead, after conversion from erg to GeV units. If the larger and seemingly erroneous value is actually used, it would imply energies an order of magnitude higher than in the calculations presented here. Predictions from this include earlier light curve cutoffs, as energies become insufficient after less time has passed, and potentially smaller separation between charm, pion and kaon components, because at each point in time, only lower energy hadrons are available for neutrino production, resulting in a depression of otherwise possible peak values. A comparison to [15] shows that figure 7 displays both of these features. Smaller injection energies further imply lower charm decay contributions to the total neutrino fluence, which figure 8 seems to support as well when compared to [15]. Adding to this concern is the large divergence from figures 4 and 5 that most likely stems from the optical depth. Setting this factor to be constant supposes a fixed fraction of protons colliding to produce hadrons, independent from density changes due to an expanding ejecta volume. Such an assumption is difficult to justify, with the potential exception of extremely high densities. As reference [15] explicitly includes an optical depth in the same way this thesis does, it is unclear how the wide disparities between neutrino spectra come about, especially considering that figures 7 and 8 without \mathcal{O} present better matches than figures 4 and 5 with \mathcal{O} to those in [15]. This issue represents a major incongruence and warrants further scrutiny, which the following chapter discusses in more detail. Due to their agreement with prior expectations and to extract physical implications from the results, calculations without optical depth are treated as though they were valid in the subsequent paragraphs.

4 Results

Examination of figure 7 confirms that charm decays exceed pion and kaon contributions at earlier times. Peak flux values for $E_\nu = 10^9$ GeV are of similar magnitude, though pions experience stronger suppression from cooling when compared to kaons. Inclusion of secondary muons as indicated by [15] would lead to increased maxima, especially for neutrinos from pion decay, but does not significantly influence the relative peak positions. At lower energies, cooling factors approaching unity lead to pions becoming dominant, with kaons slightly below that. Neutrinos from charmed hadrons are now suppressed due to their lower production cross sections and branching ratios. The opposite behavior is seen as energies become larger, with contributions from charm dominating over those from pions and kaons. Light curves in figure 7 are shaped by cooling factors at early times when all fluxes are suppressed, increase towards their maximum as decay and cooling timescales are equal, and subsequently decrease due to less protons being available. At later times, as E_p approaches E_h and hadron production is inhibited by energy conservation, a sharp cutoff is observed in the fluxes. These are universal characteristics, with charm, kaon and pion components being shifted with respect to each other as a result of their different masses and lifetimes. Besides changing their magnitudes, flux curves move towards earlier times at higher energies according to cooling and cutoff thresholds, with relative positions between individual contributions remaining mostly unaffected. The findings described so far are in agreement with results from [15].

To evaluate the fluence, figure 8 presents different time intervals, scaled by the squared neutrino energy. From the flux properties follows that charm decays dominate at earlier times, followed by kaons and pions. As the available proton energy reduces with time, each component contributes significantly at different energies, with neutrino fluence from charmed hadrons being the most energetic. Lower energies are found for kaons, while pions comprise the lowest energy part. Regarding magnitudes of the neutrino fluences, pion decay represents the largest contribution up to around $E_\nu = 10^8$ GeV energies, beyond which kaons begin to dominate. The fluence from charmed hadrons is relevant above $E_\nu = 10^9$ GeV as a threshold. Imposed by the maximum proton energy is $E_\nu = 10^{12}$ GeV as a hard cutoff, which is not visible in figure 8 for improved readability. Contrary to what [15] shows, neutrinos from charm start decreasing closer to the kaon component, with kaons being approximately equal to the lower uncertainty bound for charmed hadrons at high energies. It is therefore unclear if a charmed neutrino component is unambiguously separable from pions and kaons. As discussed previously, this can likely be traced back to the larger maximum proton energy given in [15].

4 Results

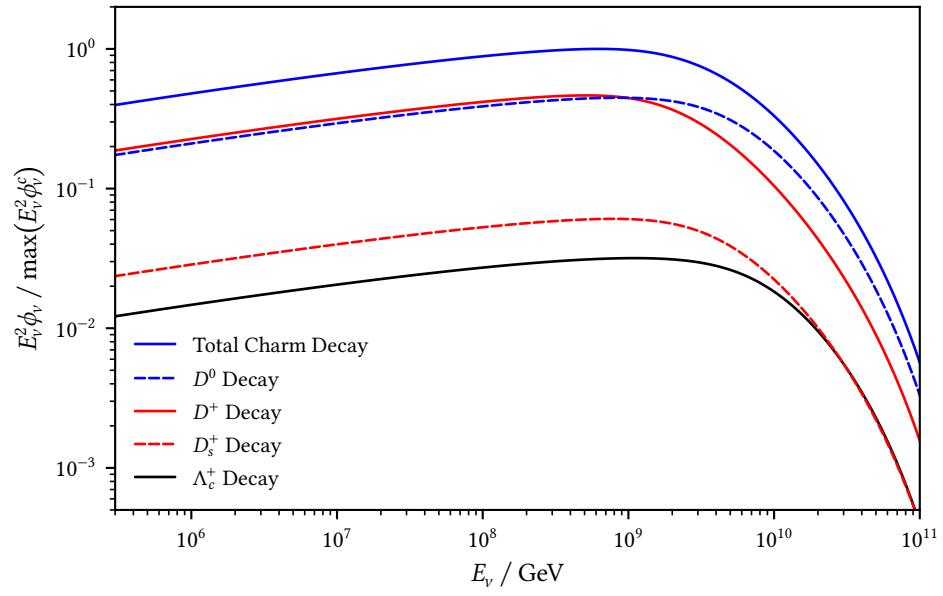


FIGURE 9: Comparison of individual charmed hadron contributions to the total charm neutrino fluence from an AGN accretion disk.

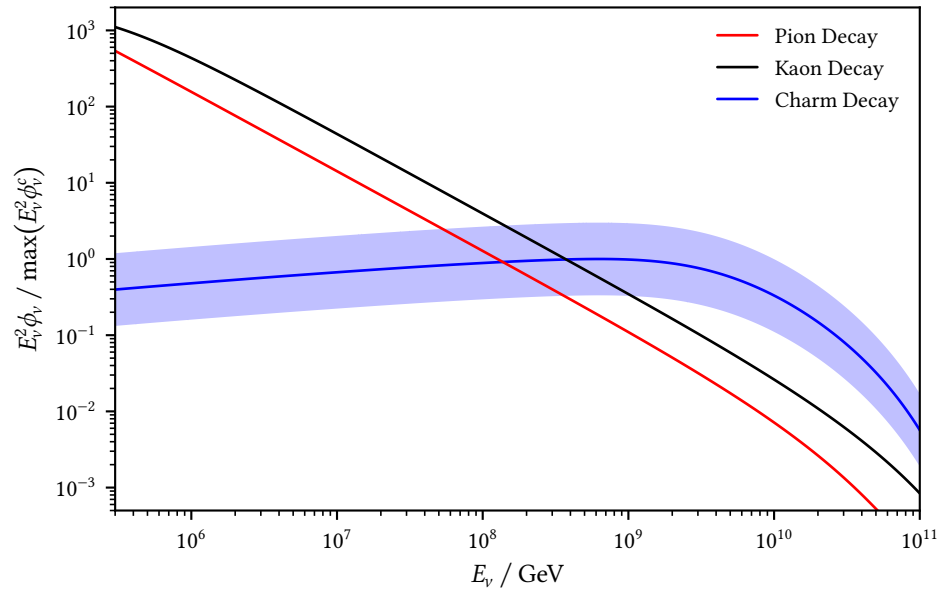


FIGURE 10: Expected neutrino fluence normalized to the maximum charmed hadron contribution from an AGN accretion disk.

5 Conclusion & Outlook

Bibliography

- [1] P. Mészáros, D. B. Fox, C. Hanna, K. Murase, *Nature Reviews Physics* **1**, 585–599, ISSN: 2522-5820, DOI: [10.1038/s42254-019-0101-z](https://doi.org/10.1038/s42254-019-0101-z), arXiv: [1906.10212](https://arxiv.org/abs/1906.10212) [[astro-ph.HE](#)] (2019).
- [2] A. A. Halim *et al.*, DOI: [10.48550/arXiv.2211.16020](https://doi.org/10.48550/arXiv.2211.16020), arXiv: [2211.16020](https://arxiv.org/abs/2211.16020) [[astro-ph.HE](#)] (2022).
- [3] A. M. Hillas, *Annual Review of Astronomy and Astrophysics* **22**, 425–444, DOI: [10.1146/annurev.aa.22.090184.002233](https://doi.org/10.1146/annurev.aa.22.090184.002233) (1984).
- [4] J. B. Tjus, L. Merten, DOI: [10.48550/arXiv.2002.00964](https://doi.org/10.48550/arXiv.2002.00964), arXiv: [2002.00964](https://arxiv.org/abs/2002.00964) [[astro-ph.HE](#)] (2020).
- [5] S. Gabici, C. Evoli, D. Gaggero, P. Lipari, P. Mertsch, E. Orlando, A. Strong, A. Vittino, *International Journal of Modern Physics D* **28**, 1930022, ISSN: 1793-6594, DOI: [10.1142/s0218271819300222](https://doi.org/10.1142/s0218271819300222), arXiv: [1903.11584](https://arxiv.org/abs/1903.11584) [[astro-ph.HE](#)] (2019).
- [6] L. O. Drury, *Astroparticle Physics* **39–40**, 52–60, ISSN: 0927-6505, DOI: [10.1016/j.astropartphys.2012.02.006](https://doi.org/10.1016/j.astropartphys.2012.02.006), arXiv: [1203.3681](https://arxiv.org/abs/1203.3681) [[astro-ph.HE](#)] (2012).
- [7] M. G. Aartsen *et al.*, *Science* **342**, 1242856, DOI: [10.1126/science.1242856](https://doi.org/10.1126/science.1242856), arXiv: [1311.5238](https://arxiv.org/abs/1311.5238) [[astro-ph.HE](#)] (2013).
- [8] M. G. Aartsen *et al.*, *The Astrophysical Journal* **833**, 3, ISSN: 1538-4357, DOI: [10.3847/0004-637x/833/1/3](https://doi.org/10.3847/0004-637x/833/1/3), arXiv: [1607.08006](https://arxiv.org/abs/1607.08006) [[astro-ph.HE](#)] (2016).
- [9] B. P. Abbott *et al.*, *Physical Review Letters* **116**, ISSN: 1079-7114, DOI: [10.1103/physrevlett.116.061102](https://doi.org/10.1103/physrevlett.116.061102), arXiv: [1602.03837](https://arxiv.org/abs/1602.03837) [[gr-qc](#)] (2016).
- [10] J. K. Becker, *Physics Reports* **458**, 173–246, ISSN: 0370-1573, DOI: [10.1016/j.physrep.2007.10.006](https://doi.org/10.1016/j.physrep.2007.10.006), arXiv: [0710.1557](https://arxiv.org/abs/0710.1557) [[astro-ph](#)] (2008).
- [11] M. Aartsen *et al.*, *Science* **361**, ISSN: 1095-9203, DOI: [10.1126/science.aat1378](https://doi.org/10.1126/science.aat1378), arXiv: [1807.08816](https://arxiv.org/abs/1807.08816) [[astro-ph.HE](#)] (2018).
- [12] M. Aartsen *et al.*, *Science* **361**, 147–151, ISSN: 1095-9203, DOI: [10.1126/science.aat2890](https://doi.org/10.1126/science.aat2890), arXiv: [1807.08794](https://arxiv.org/abs/1807.08794) [[astro-ph.HE](#)] (2018).
- [13] K. Murase, P. Mészáros, B. Zhang, *Physical Review D* **79**, ISSN: 1550-2368, DOI: [10.1103/physrevd.79.103001](https://doi.org/10.1103/physrevd.79.103001), arXiv: [0904.2509](https://arxiv.org/abs/0904.2509) [[astro-ph.HE](#)] (2009).
- [14] J. Becker Tjus, W. Rhode, at European Physical Journal Web of Conferences, vol. 290, 10002, 10002, DOI: [10.1051/epjconf/202329010002](https://doi.org/10.1051/epjconf/202329010002).
- [15] J. A. Carpio, K. Murase, M. H. Reno, I. Sarcevic, A. Stasto, *Physical Review D* **102**, ISSN: 2470-0029, DOI: [10.1103/PhysRevD.102.103001](https://doi.org/10.1103/PhysRevD.102.103001), arXiv: [2007.07945](https://arxiv.org/abs/2007.07945) [[astro-ph.HE](#)] (2020).
- [16] P. D. Group *et al.*, *Progress of Theoretical and Experimental Physics* **2022**, 083C01, ISSN: 2050-3911, DOI: [10.1093/ptep/ptac097](https://doi.org/10.1093/ptep/ptac097) (2022).
- [17] T. K. Gaisser, R. Engel, E. Resconi, *Cosmic Rays and Particle Physics* (Cambridge University Press, Cambridge, Second Edition, 2016), ISBN: 9781139192194, DOI: [10.1017/CBO9781139192194](https://doi.org/10.1017/CBO9781139192194).

Bibliography

- [18] M. S. Longair, *High Energy Astrophysics* (Cambridge University Press, Cambridge, Third Edition, 2011), ISBN: 9780511778346, DOI: [10.1017/CBO9780511778346](https://doi.org/10.1017/CBO9780511778346).
- [19] C. Thompson, R. C. Duncan, *The Astrophysical Journal* **408**, 194, DOI: [10.1086/172580](https://doi.org/10.1086/172580) (1993).
- [20] B. Haskell, A. Sedrakian, in *Astrophysics and Space Science Library* (Springer International Publishing, 2018), Chapter 8, 401–454, ISBN: 9783319976167, ISSN: 2214-7985, arXiv: [1709.10340](https://arxiv.org/abs/1709.10340) [[astro-ph.HE](#)].
- [21] Y. Sang, G. Chanmugam, *Astrophysical Journal* **363**, 597, DOI: [10.1086/169369](https://doi.org/10.1086/169369) (1990).
- [22] P. Haensel, J. P. Lasota, J. L. Zdunik, DOI: [10.48550/arXiv.astro-ph/9901118](https://doi.org/10.48550/arXiv.astro-ph/9901118), arXiv: [astro-ph/9901118](https://arxiv.org/abs/astro-ph/9901118) [[astro-ph](#)] (1999).
- [23] C. Alvarez, A. Carramiñana, *Astronomy & Astrophysics* **414**, 651–658, ISSN: 1432-0746, DOI: [10.1051/0004-6361:20031627](https://doi.org/10.1051/0004-6361:20031627), arXiv: [astro-ph/0311267](https://arxiv.org/abs/astro-ph/0311267) (2004).
- [24] A. J. Deutsch, *Annales d’Astrophysique* **18**, 1 (1955).
- [25] J. D. Jackson, *Classical Electrodynamics* (Wiley, New York, NY, Third Edition, 1999), ISBN: 9780471309321.
- [26] A. Gruzinov, *The Astrophysical Journal* **647**, L119–L122, ISSN: 1538-4357, DOI: [10.1086/506590](https://doi.org/10.1086/506590), arXiv: [astro-ph/0510751](https://arxiv.org/abs/astro-ph/0510751) (2006).
- [27] A. Spitkovsky, *The Astrophysical Journal* **648**, L51–L54, ISSN: 1538-4357, DOI: [10.1086/507518](https://doi.org/10.1086/507518), arXiv: [astro-ph/0603147](https://arxiv.org/abs/astro-ph/0603147) (2006).
- [28] P. Goldreich, W. H. Julian, *Astrophysical Journal* **157**, 869, DOI: [10.1086/150119](https://doi.org/10.1086/150119) (1969).
- [29] J. Li, A. Spitkovsky, A. Tchekhovskoy, *The Astrophysical Journal* **746**, 60, DOI: [10.1088/0004-637X/746/1/60](https://doi.org/10.1088/0004-637X/746/1/60), arXiv: [1107.0979](https://arxiv.org/abs/1107.0979) [[astro-ph.HE](#)] (2012).
- [30] S. E. Gralla, N. Iqbal, *Physical Review D* **99**, ISSN: 2470-0029, DOI: [10.1103/physrevd.99.105004](https://doi.org/10.1103/physrevd.99.105004), arXiv: [1811.07438](https://arxiv.org/abs/1811.07438) [[hep-th](#)] (2019).
- [31] M. Visser, DOI: [10.48550/arXiv.0706.0622](https://doi.org/10.48550/arXiv.0706.0622), arXiv: [0706.0622](https://arxiv.org/abs/0706.0622) [[gr-qc](#)] (2008).
- [32] R. Blandford, D. Meier, A. Readhead, *Annual Review of Astronomy and Astrophysics* **57**, 467–509, ISSN: 1545-4282, DOI: [10.1146/annurev-astro-081817-051948](https://doi.org/10.1146/annurev-astro-081817-051948), arXiv: [1812.06025](https://arxiv.org/abs/1812.06025) [[astro-ph.HE](#)] (2019).
- [33] M. A. Abramowicz, P. C. Fragile, *Living Reviews in Relativity* **16**, ISSN: 1433-8351, DOI: [10.12942/lrr-2013-1](https://doi.org/10.12942/lrr-2013-1), arXiv: [1104.5499](https://arxiv.org/abs/1104.5499) [[astro-ph.HE](#)] (2013).
- [34] V. Beckmann, C. R. Shrader, DOI: [10.48550/arXiv.1302.1397](https://doi.org/10.48550/arXiv.1302.1397), arXiv: [1302.1397](https://arxiv.org/abs/1302.1397) [[astro-ph.HE](#)] (2013).
- [35] K. Murase, F. W. Stecker, in *The Encyclopedia of Cosmology* (WORLD SCIENTIFIC, 2023), 483–540, ISBN: 9789811282645, DOI: [10.1142/9789811282645_0010](https://doi.org/10.1142/9789811282645_0010), arXiv: [2202.03381](https://arxiv.org/abs/2202.03381) [[astro-ph.HE](#)].
- [36] B. Eichmann, F. Oikonomou, S. Salvatore, R.-J. Dettmar, J. B. Tjus, *The Astrophysical Journal* **939**, 43, ISSN: 1538-4357, DOI: [10.3847/1538-4357/ac9588](https://doi.org/10.3847/1538-4357/ac9588), arXiv: [2207.00102](https://arxiv.org/abs/2207.00102) [[astro-ph.HE](#)] (2022).
- [37] V. Belousov, V. Ezhela, Y. Kuyanov, N. Tkachenko, *Physics of Atomic Nuclei* **79**, 113–117, DOI: [10.1134/S1063778816010075](https://doi.org/10.1134/S1063778816010075) (2016).
- [38] D. Fagundes, M. Menon, *Nuclear Physics A* **880**, 1–11, ISSN: 0375-9474, DOI: [10.1016/j.nuclphysa.2012.01.017](https://doi.org/10.1016/j.nuclphysa.2012.01.017), arXiv: [1112.5115](https://arxiv.org/abs/1112.5115) [[hep-ph](#)] (2012).
- [39] D. A. Fagundes, M. J. Menon, P. V. R. G. Silva, *Journal of Physics G: Nuclear and Particle Physics* **40**, 065005, ISSN: 1361-6471, DOI: [10.1088/0954-3899/40/6/065005](https://doi.org/10.1088/0954-3899/40/6/065005), arXiv: [1208.3456](https://arxiv.org/abs/1208.3456) [[hep-ph](#)] (2013).

Bibliography

- [40] M. Froissart, *Phys. Rev.* **123**, 1053–1057, DOI: [10.1103/PhysRev.123.1053](https://doi.org/10.1103/PhysRev.123.1053) (3 1961).
- [41] V. P. Gonçalves, M. V. Machado, *Journal of High Energy Physics* **2007**, 028–028, ISSN: 1029-8479, DOI: [10.1088/1126-6708/2007/04/028](https://doi.org/10.1088/1126-6708/2007/04/028), arXiv: [hep-ph/0607125](https://arxiv.org/abs/hep-ph/0607125) (2007).
- [42] A. Bhattacharya, R. Enberg, M. H. Reno, I. Sarcevic, A. Stasto, *Journal of High Energy Physics* **2015**, ISSN: 1029-8479, DOI: [10.1007/jhep06\(2015\)110](https://doi.org/10.1007/jhep06(2015)110), arXiv: [1502.01076](https://arxiv.org/abs/1502.01076) [[hep-ph](#)] (2015).
- [43] R. Aaij *et al.*, *Journal of High Energy Physics* **2016**, [Erratum: JHEP 09, 013 (2016), Erratum: JHEP 05, 074 (2017)], 159, DOI: [10.1007/JHEP03\(2016\)159](https://doi.org/10.1007/JHEP03(2016)159), arXiv: [1510.01707](https://arxiv.org/abs/1510.01707) [[hep-ex](#)] (2016).
- [44] A. Metz, A. Vossen, *Progress in Particle and Nuclear Physics* **91**, 136–202, ISSN: 0146-6410, DOI: [10.1016/j.pnpnp.2016.08.003](https://doi.org/10.1016/j.pnpnp.2016.08.003), arXiv: [1607.02521](https://arxiv.org/abs/1607.02521) [[hep-ex](#)] (2016).
- [45] B. A. Kniehl, G. Kramer, *Physical Review D* **74**, ISSN: 1550-2368, DOI: [10.1103/physrevd.74.037502](https://doi.org/10.1103/physrevd.74.037502), arXiv: [hep-ph/0607306](https://arxiv.org/abs/hep-ph/0607306) (2006).
- [46] S. R. Kelner, F. A. Aharonian, V. V. Bugayov, *Phys. Rev. D* **74**, 034018, DOI: [10.1103/PhysRevD.74.034018](https://doi.org/10.1103/PhysRevD.74.034018), arXiv: [astro-ph/0606058](https://arxiv.org/abs/astro-ph/0606058) (3 2006).
- [47] A. Bhattacharya, R. Enberg, Y. S. Jeong, C. Kim, M. H. Reno, I. Sarcevic, A. Stasto, *Journal of High Energy Physics* **2016**, ISSN: 1029-8479, DOI: [10.1007/jhep11\(2016\)167](https://doi.org/10.1007/jhep11(2016)167), arXiv: [1607.00193](https://arxiv.org/abs/1607.00193) [[hep-ph](#)] (2016).
- [48] M. Lisovyi, A. Verbytskyi, O. Zenaiev, *The European Physical Journal C* **76**, ISSN: 1434-6052, DOI: [10.1140/epjc/s10052-016-4246-y](https://doi.org/10.1140/epjc/s10052-016-4246-y), arXiv: [1509.01061](https://arxiv.org/abs/1509.01061) [[hep-ex](#)] (2016).
- [49] E. V. Bugaev, A. Misaki, V. A. Naumov, T. S. Sinigovskaya, S. I. Sinigovsky, N. Takahashi, *Physical Review D* **58**, ISSN: 1089-4918, DOI: [10.1103/physrevd.58.054001](https://doi.org/10.1103/physrevd.58.054001), arXiv: [hep-ph/9803488](https://arxiv.org/abs/hep-ph/9803488) (1998).
- [50] G. I. Lykasov, A. I. Malakhov, A. A. Zaitsev, *The European Physical Journal A* **57**, ISSN: 1434-601X, DOI: [10.1140/epja/s10050-021-00408-9](https://doi.org/10.1140/epja/s10050-021-00408-9), arXiv: [2012.02451](https://arxiv.org/abs/2012.02451) [[hep-ph](#)] (2021).
- [51] G. I. Lykasov, A. I. Malakhov, A. A. Zaitsev, *The European Physical Journal A* **58**, ISSN: 1434-601X, DOI: [10.1140/epja/s10050-022-00773-z](https://doi.org/10.1140/epja/s10050-022-00773-z), arXiv: [2201.10301](https://arxiv.org/abs/2201.10301) [[hep-ph](#)] (2022).
- [52] H. B. J. Koers, A. Pe’er, R. A. M. J. Wijers, arXiv: [hep-ph/0611219](https://arxiv.org/abs/hep-ph/0611219) (2006).